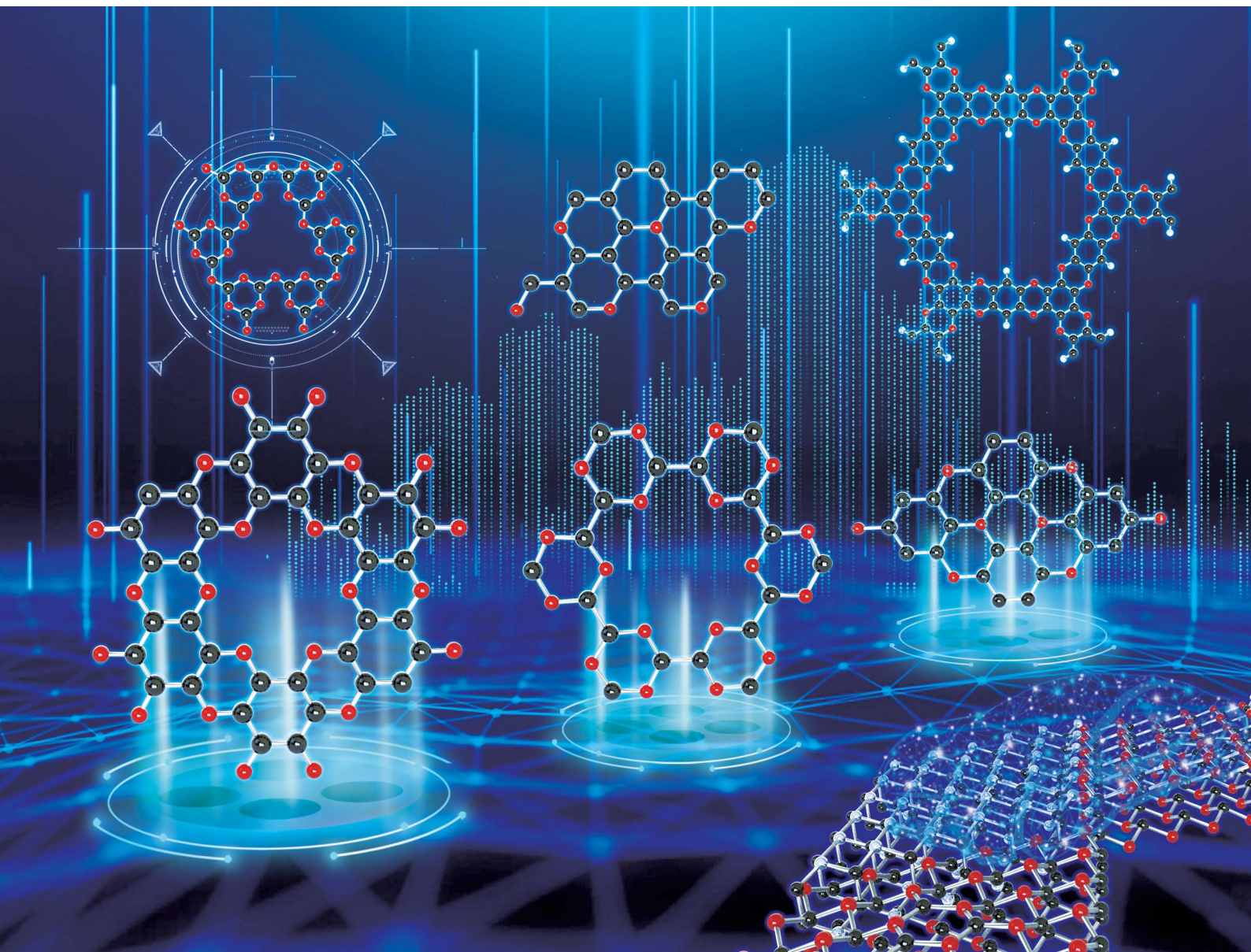


# Journal of Materials Chemistry A

Materials for energy and sustainability

[rsc.li/materials-a](https://rsc.li/materials-a)



ISSN 2050-7488

**REVIEW ARTICLE**

Zhimin Ao, Shaobin Wang *et al.*  
Novel two-dimensional crystalline carbon nitrides beyond  
g-C<sub>3</sub>N<sub>4</sub>: structure and applications

Cite this: *J. Mater. Chem. A*, 2021, 9, 17

# Novel two-dimensional crystalline carbon nitrides beyond g-C<sub>3</sub>N<sub>4</sub>: structure and applications

Li Tan,<sup>†a</sup> Chunyang Nie,<sup>†a</sup> Zhimin Ao,<sup>ID</sup>\*<sup>a</sup> Hongqi Sun,<sup>ID</sup><sup>b</sup> Taicheng An<sup>ID</sup><sup>a</sup> and Shaobin Wang<sup>ID</sup>\*<sup>c</sup>

Two-dimensional (2D) crystalline carbon nitrides (C<sub>x</sub>N<sub>y</sub>) with graphene-like atomic structures but semiconducting nature are new appealing materials, and increasing interest has been focused on their synthesis, properties, and applications. Apart from the well-known graphitic carbon nitride (g-C<sub>3</sub>N<sub>4</sub>), other types of 2D C<sub>x</sub>N<sub>y</sub> nanocrystals including C<sub>2</sub>N, C<sub>3</sub>N and C<sub>5</sub>N<sub>2</sub> are also successfully fabricated in recent years and their properties and potential uses in various fields have been widely investigated. Meanwhile, g-CN, C<sub>2</sub>N<sub>2</sub>, C<sub>2</sub>N<sub>3</sub> and C<sub>5</sub>N have been theoretically predicted, and their properties and potential applications have also been researched. Until now, 2D crystalline C<sub>x</sub>N<sub>y</sub> compounds have demonstrated promising applications in photocatalysis, electrocatalysis, gas adsorption/separation, and energy storage devices, from both experimental and theoretical aspects, stemming from their unique geometric structures, tunable electronic properties, and high specific surface area. Herein, recent advances in the synthesis of 2D C<sub>x</sub>N<sub>y</sub> nanocrystals and their applications in various fields are summarized. Moreover, future challenges and opportunities for developing 2D C<sub>x</sub>N<sub>y</sub> nanocrystals for more broad applications including environmental remediation are also discussed.

Received 30th July 2020  
Accepted 16th September 2020

DOI: 10.1039/d0ta07437c

rsc.li/materials-a

<sup>a</sup>Guangdong Key Laboratory of Environmental Catalysis and Health Risk Control, Guangzhou Key Laboratory of Environmental Catalysis and Pollution Control, School of Environmental Science and Engineering, Institute of Environmental Health and Pollution Control, Guangdong University of Technology, Guangdong, 510006, China. E-mail: zhimin.ao@gdut.edu.cn

<sup>b</sup>School of Engineering, Edith Cowan University, Joondalup, WA 6027, Australia

<sup>c</sup>School of Chemical Engineering and Advanced Materials, The University of Adelaide, Adelaide, SA 5005, Australia. E-mail: Shaobin.wang@adelaide.edu.au

<sup>†</sup> These authors contributed equally to this work.

## 1. Introduction

Graphene, as a two-dimensional (2D) atomic crystal available to the scientific community, was successfully discovered by Novoselov in 2004.<sup>1</sup> An ideal graphene structure is composed of a single layer of sp<sup>2</sup>-hybridized carbon atoms.<sup>2</sup> Ever since, the applications of this new material have been developed rapidly in many fields such as electronics, photonics, energy storage and conversion, and environmental remediation, arising from its superior electrical and thermal conductivity, chemical stability, mechanical stiffness, and other physical and chemical



nitride-based catalysts for the adsorption of volatile organic compounds and their catalytic remediation.

Miss Li Tan obtained her Master's degree in 2018 from Yanshan University (China) and she is now pursuing a PhD degree under the supervision of Prof. Zhimin Ao at the School of Environmental Science and Engineering, Institute of Environmental Health and Pollution Control, Guangdong University of Technology. Her current research interests focus on the synthesis of novel 2D carbon-



carbon-based catalysts for aqueous organic pollutant remediation and catalytic mechanisms.

Dr Chunyang Nie obtained her Master's degree in 2013 from East China Normal University (China) and PhD degree in 2016 from Universite Paul Sabatier (France) under the supervision of Dr Emmanuel Flahaut and Dr Marc Monthieux. She joined Prof. Ao's group at the Guangdong University of Technology in 2016 as a Postdoctoral Fellow. Her current research interests focus on the synthesis of novel

properties.<sup>3</sup> For instance, graphene has been widely studied as an appealing adsorbent for hazardous gases like volatile organic compounds (VOCs), CO<sub>2</sub> and aqueous organic pollutants due to its high theoretical specific surface area (SSA, 2630 m<sup>2</sup> g<sup>-1</sup>).<sup>4</sup> Additionally, the unique 2D planar structure, large SSA, good electrical conductivity and chemical stability also make graphene an excellent catalyst and support in various catalytic reactions for environmental remediation.<sup>4</sup> Moreover, the discovery of graphene has triggered research interest in many other 2D materials.

Regardless of the above merits, the zero-bandgap feature of graphene impeded its further applications in electronic devices like switches and light-emitting diodes, and photocatalysis.<sup>5</sup> In order to open the bandgap of graphene, diverse structural modifications involving cutting graphene into narrow

nanoribbons and doping with heteroelements have been attempted.<sup>6</sup> Among them, doping with N atoms is a good option due to the similar relative atomic mass and electron configuration of the N element to the C element, enabling the feasible fitting of N atoms into the covalent carbon matrix.<sup>7</sup> However, this chemical modification can inevitably lead to certain damage to the 2D carbon lattice of pristine graphene and the stoichiometry between C and N cannot be easily controlled *via* the top-down approach.<sup>8</sup> With the motivation to supplement the electronic properties of the graphene system with other 2D materials that show similar atomic crystalline structures and intrinsic semiconductivity, bottom-up approaches with C-rich and N-rich precursors to fabricate 2D atomic carbon nitride (C<sub>x</sub>N<sub>y</sub>) crystals have been given much attention.<sup>9</sup>



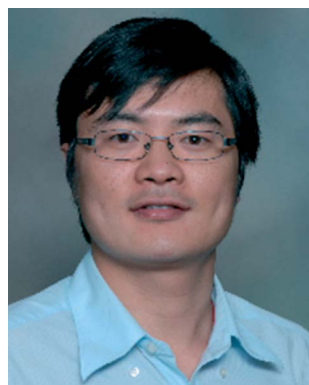
*Prof. Zhimin Ao received his PhD in Materials Science from Jilin University, China in 2008. He is currently a full professor at the Institute of Environmental Health and Pollution Control, School of Environmental Science and Engineering, Guangdong University of Technology. His research interests mainly focus on the development of environmental catalysts and corresponding mechanism*

*investigation. He has published over 130 SCI papers with citations over 4800 times and an H index of 31. He serves as an Associate Editor of Frontiers in Nanotechnology.*



*Prof. Taicheng An received his PhD in Environmental Science from Sun Yat-sen University, China in 2002. He is currently a full professor and the director of the Institute of Environmental Health and Pollution Control, Guangdong University of Technology. His research interests mainly focus on: (1) synthesis, characterization, optimization and application of nano-structured catalysts and natural*

*mineral materials in environmental remediation; (2) applications of advanced oxidation processes (AOPs); (3) the transportation mechanisms, fate prediction and health effect of emerging organic contaminants. He has been awarded over 70 patents and published over 380 refereed research papers. He serves as an Associate Editor of Appl. Catal. B: Environ. and Ctr. Rev. Env. Tech.*



*Prof. Hongqi Sun received his PhD degree in Chemical Engineering in 2008 from Nanjing University of Technology, China. He joined Edith Cowan University (ECU) in March 2016 and became a full Professor of Chemical Engineering at ECU in November 2017. His research focuses on novel catalysis (photocatalysis, photo-thermal catalysis, photo-electrochemical catalysis, and*

*membrane catalysis) and advanced oxidation processes (AOPs) over nanostructured materials for solar-to-chemical conversion and environmental remediation. He serves as the Associate Editor of RSC Advances, and Speciality Chief Editor of Frontiers of Nanotechnology, assessor of ARC, committee member of international conferences, and referee of international journals.*



*Prof. Shaobin Wang obtained his PhD in Chemical Engineering from the University of Queensland, Australia. He is now a Professor at the School of Chemical Engineering and Advanced Materials, The University of Adelaide, Australia. His research interests focus on nanomaterial synthesis and application for adsorption and catalysis, fuel and energy conversion and environmental*

*remediation. He has published more than 400 refereed journal papers with citations over 40 000 and an H-index of 113. He is a Global Highly Cited Researcher in Engineering in 2016–2019.*

Research on  $C_xN_y$  was mainly stimulated by the theoretical work of Lu and Cohen in 1989, which postulated that a carbon(IV) nitride ( $sp^3$ -hybridized) crystal should show comparable or higher hardness than diamond.<sup>10</sup> Since then, an exponentially growing number of publications exploring novel  $C_xN_y$  materials from both experimental and theoretical aspects have been reported, while most of them focused on the 3D  $C_xN_y$ -phases and few of them on the 2D crystalline  $C_xN_y$  materials. It was not until 2009 that polymeric graphitic- $C_3N_4$  ( $g-C_3N_4$ ) was demonstrated as an excellent visible-light-responsive photocatalyst,<sup>11</sup> since then more and more efforts have been devoted to the synthesis of 2D  $g-C_3N_4$  nanosheets *via* exfoliation of bulk  $g-C_3N_4$  in order to further enhance the photocatalytic performance.<sup>12</sup> Recently, the experimental successes in 2D  $C_2N$  and  $C_3N$  crystals pushed the research of 2D  $C_xN_y$  materials to a new high level.<sup>13</sup> A large number of attempts have been made on the preparation and potential applications of these new 2D materials as well as prediction of other types of 2D  $C_xN_y$  atomic crystals such as  $C_2N_2$  and  $C_5N_2$ .<sup>14</sup>

Currently, 2D  $C_xN_y$  materials show great potential in field-effect transistors (FETs) owing to their semiconducting character, which complements the uses of graphene and insulating 2D boron nitride crystals.<sup>13</sup> Meanwhile, the inherent bandgap of 2D  $C_xN_y$  materials makes them potential environment-friendly photocatalysts for different reactions like water splitting, degradation of organic pollutants,  $CO_2$  reduction reaction ( $CO_2RR$ ) and so on. Additionally, the introduction of N atoms into the carbon matrix can also break the inertness of pristine graphene and create Lewis basic sites, providing 2D  $C_xN_y$  with good catalytic activity in different reactions. Analogous to graphene, 2D  $C_xN_y$  materials show high theoretical SSAs, good chemical stability and other similar physicochemical properties as well.<sup>15</sup> Therefore, they are considered as outstanding adsorbents for gas adsorption and catalyst supports for loading uniformly dispersed nanoparticles.<sup>9c,16</sup> In particular, the N atoms in the  $C_xN_y$  network can serve as anchoring sites for isolated metal atoms or dimers, leading to the formation of single atom catalysts (SACs) or double-atom catalysts as a hot topic in recent years.<sup>17</sup>

To date, a diversity of 2D  $C_xN_y$  materials with different stoichiometric ratios between C and N have been documented in the literature, which include  $g-C_3N_4$ , CN,  $C_2N$ ,  $C_3N$ ,  $C_2N_2$ ,  $C_2N_3$ ,  $C_5N$  and  $C_5N_2$ . For these  $C_xN_y$  compounds, the arrangements of C and N atoms in a basic benzene ring and the corresponding structural motif in the  $sp^2$ -hybridized basal plane differ from each other (the structures of these  $C_xN_y$  materials are shown in Fig. 1). As a result, they exhibit distinct physicochemical properties with respect to the bandgap and texture. Among them,  $g-C_3N_4$ ,  $C_2N$  and  $C_3N$  have aroused much interest in the field of photocatalysis because they have been already synthesized in laboratories and possess a suitable bandgap and good visible-light adsorption, while the rest of the 2D  $C_xN_y$  compounds are still in the theoretical research stage.

In this work, we present a comprehensive overview of the recent progress in 2D  $C_xN_y$  research. Considering a large quantity of reviews on 2D  $g-C_3N_4$  in the literature,<sup>12a</sup> herein, we will focus on the other members of 2D  $C_xN_y$ , except  $g-C_3N_4$ ,

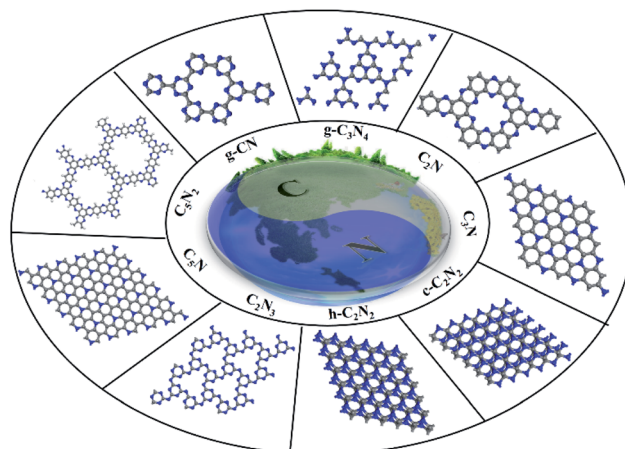


Fig. 1 The structures of different 2D  $C_xN_y$  compounds, including  $g-CN$ ,  $g-C_3N_4$ ,  $C_2N$ ,  $C_3N$ ,  $c-C_2N_2$ ,  $h-C_2N_2$ ,  $C_2N_3$ ,  $C_5N$  and  $C_5N_2$ .

including  $g-CN$ ,  $C_2N$ ,  $C_3N$ ,  $C_2N_2$ ,  $C_2N_3$ ,  $C_5N$  and  $C_5N_2$ . In Sections 2–4, we describe the structural characteristics, experimental synthesis, intrinsic properties and applications (practical and simulated) of  $C_2N$ ,  $C_3N$  and  $g-CN$ , respectively. In Section 5, we will discuss the crystalline structure, electronic properties, and possible applications of  $C_2N_2$ ,  $C_2N_3$ ,  $C_5N$  and  $C_5N_2$ . Finally, we go beyond the fundamental properties of these 2D  $C_xN_y$  materials and give an outlook of the promising applications of such materials in more areas including environmental remediation in future.

## 2. $C_2N$

As early as 1998, Komatsu and Samejima reported the fabrication of amorphous  $C_xN_y$  with a random-layer structure and a chemical composition of  $C_2N$  through the shock-wave compression of a C- and N-containing polymer.<sup>18</sup> In the later decade, little effort was devoted to the synthesis of the 2D  $C_2N$  crystal. In 2015, Baek *et al.* demonstrated the successful preparation of a 2D  $C_2N$  crystal and its crystalline structure with the assistance of advanced characterization tools. Afterwards, a large quantity of experimental and computational studies on 2D  $C_2N$  have been published due to its peculiar structure and physicochemical properties. In this section, the crystalline structure, synthetic methods, electronic properties, and applications of 2D  $C_2N$  are summarized.

### 2.1 Crystalline structure of $C_2N$

A  $C_2N$  monolayer can be considered as a nitrogenated holey graphene layer, in which the benzene rings are connected by nitrogen atoms to constitute large six-membered aromatic rings with two nitrogen atoms facing each other, leading to the formation of periodically uniform holes (Fig. 2).<sup>19</sup> All the N atoms in the 2D  $C_2N$  structure belong to 'pyridine-type' or 'pyrazine-type' N.<sup>9a</sup> The primitive cell of the  $C_2N$  monolayer is shown in Fig. 2, in which three bonds with different lengths are labeled.<sup>20</sup> The optimized lattice parameter (the inter-hole distance) is determined to be 8.30 Å by density functional

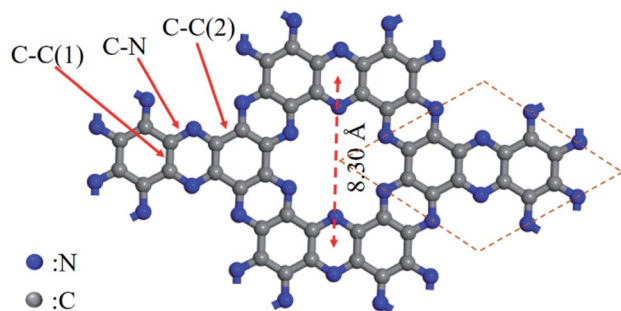


Fig. 2 The monolayer structure of the  $C_2N$  cell.

theory (DFT) calculations. However, the lengths of C–N, C–C (1) and C–C (2) bonds vary slightly in different theoretical studies. For instance, Du *et al.*<sup>21</sup> reported that the lengths of C–N, C–C (1) and C–C (2) bonds were calculated to be 1.336 Å, 1.429 Å and 1.470 Å, respectively, whereas Gong *et al.*<sup>20</sup> proposed that the lengths of the three bonds were estimated to be 1.339 Å, 1.432 Å, and 1.469 Å, respectively.

## 2.2 Synthesis of $C_2N$

The first synthesis report of the 2D  $C_2N$  crystal was given by Baik and co-workers in 2015<sup>9a</sup> using the wet-chemical reaction of hexaaminobenzene (HAB) trihydrochloride and hexaketocyclohexane (HKH) octahydrate in *N*-methyl-2-pyrrolidone (NMP) with sulphuric acid or trifluoromethanesulphonic acid. Due to the spontaneous polycondensation between HAB and HKH, a layered crystalline 2D network structure was formed

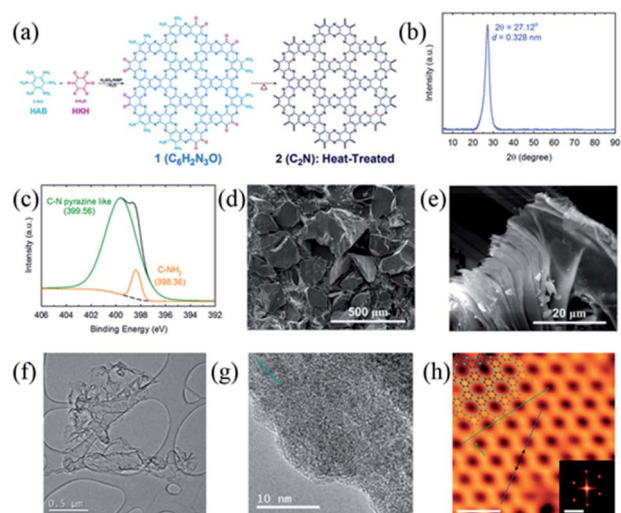


Fig. 3 The schematic representation of the  $C_2N$ -h2D crystal and its characterization: (a) the schematic representation of the  $C_2N$ -h2D crystal; (b) XRD pattern, (c) XPS survey spectrum, (d) SEM image, and (e) SEM image of heat-treated  $C_2N$ -h2D flakes; (f) TEM image, (g) high-resolution TEM image, and (h) STM topography image of the  $C_2N$ -h2D crystal, top-left inset is the structure of the  $C_2N$ -h2D crystal superimposed on the image. The scale bars and the inset are 2.0 nm, 2.0  $nm^{-1}$ . Reprinted with permission from ref. 9a copyright 2015, Springer Nature.

(Fig. 3a), referred to as the ' $C_2N$  holey 2D crystal' or ' $C_2N$ -h2D crystal'. The 2D  $C_2N$  crystalline structure was validated by a series of characterization tools including X-ray diffraction (XRD), X-ray photoelectron spectroscopy (XPS), elemental analysis and electron microscopy (Fig. 3b–h).<sup>9a</sup>

The XRD pattern (Fig. 3b) revealed that the  $C_2N$ -h2D crystal was well-crystallized with an interlayer distance of 0.328 nm. Notably, this interspace is slightly lower than that of graphite (0.335 nm),<sup>22</sup> attributed to the stronger interlayer interactions. XPS analysis indicated the presence of  $sp^2$ -hybridized N atoms in the resultant crystals (Fig. 3c). With scanning electron microscopy (SEM, Fig. 3d), the as-prepared  $C_2N$ -h2D crystals were observed to be constituted by large and thick grains with sizes of a few hundred micrometers. Notably, a post-annealing treatment at 700 °C on the as-prepared  $C_2N$ -h2D crystals can reduce the agglomeration of the grains and thinner flakes were obtained (Fig. 3e). Meanwhile, wrinkled and transparent sheets similar to graphene were observed in the transmission electron microscopy (TEM) image of  $C_2N$ -h2D crystals (Fig. 3f) and highly crystallized microstructures of those sheets were demonstrated by the high-resolution TEM image (Fig. 3g). The interlayer distance of the  $C_2N$ -h2D crystal was measured to be 0.327 nm from the high-resolution TEM image, consistent with the XRD results. Furthermore, the evenly distributed holey structure in hexagonal arrays of a single  $C_2N$  layer as proposed by the theoretical model was unambiguously displayed by the scanning tunnelling microscopy (STM) image (Fig. 3h). The inter-hole distance of the as-prepared crystal was estimated to be  $\sim 8.24 \pm 0.96$  Å according to the STM characterization, agreeing with the theoretical calculations. In Baik's subsequent research, different metal-based chlorides ( $CoCl_2$ ,  $NiCl_2$ ,  $RuCl_3$ , etc.) were introduced into the NMP solvent and 2D  $C_2N$  supported metallic nanoparticle composites were obtained.<sup>23</sup>

More recently, Shinde and co-workers reported the preparation of  $C_2N$  aerogels ( $C_2NA$ ) *via* a similar synthetic strategy to that of the  $C_2N$ -h2D crystal, which utilized hexaaminobenzene and chloroanilic acid as precursors.<sup>19</sup> In their work, the polymerization of the two precursors in 1-methyl-2-pyrrolidinone solution was initiated by adding *L*-alanine and sulfuric acid and the mixture was heated at 120 °C to form a hydrogel. Afterwards, the hydrogel was freeze dried for 20 h and then was subjected to an annealing treatment in a  $N_2$  atmosphere at 200 °C for 30 min to eliminate the oxygenated groups in the  $C_2NA$  (Fig. 4a). Meanwhile, the authors also fabricated sulfur-modulated  $C_2NA$  (S- $C_2NA$ ) and phosphorus-modulated  $C_2NA$  (P- $C_2NA$ ) *via* a similar procedure with the extra addition of *L*-cysteine and ammonium peroxydisulfate (for the S- $C_2NA$  case) or *L*-phosphoserine and ammonium phosphate (for the P- $C_2NA$  case) for the polymerization. The good crystallinity of  $C_2NA$  and doped  $C_2NA$  is also supported by the XRD patterns (Fig. 4b). Furthermore, successful doping of P or S atoms into  $C_2NA$  was validated by XPS analysis (Fig. 4c). The as-prepared aerogels show a dark grey and sponge-like appearance and low mass density (Fig. 4d). SEM and TEM micrographs reveal that the as-prepared aerogels are composed of interweaved, twisted and crystallized  $C_2N$  nanoribbons, which exhibit widths ranging from 150–200 nm (Fig. 4e and f). Meanwhile, the STM image

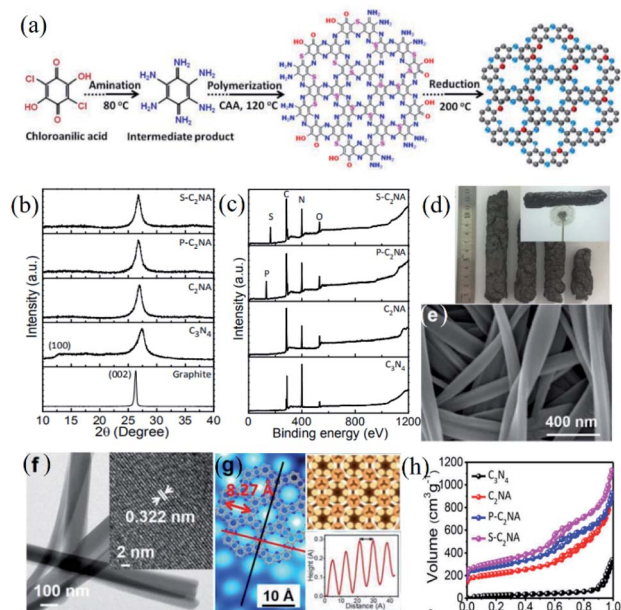


Fig. 4 (a) Schematic illustration depicting the development of the S-C<sub>2</sub>N<sub>4</sub>, (b) XRD patterns of graphite, and the pristine C<sub>3</sub>N<sub>4</sub>, C<sub>2</sub>N<sub>4</sub>, P-C<sub>2</sub>N<sub>4</sub>, and S-C<sub>2</sub>N<sub>4</sub>, and (c) survey scans of the XPS spectra of pristine C<sub>3</sub>N<sub>4</sub>, C<sub>2</sub>N<sub>4</sub>, P-C<sub>2</sub>N<sub>4</sub>, and S-C<sub>2</sub>N<sub>4</sub>. (d) Optical image of the fabricated S-C<sub>2</sub>N<sub>4</sub>; the inset shows the ultralight aerogel suspended on a dandelion, (e) SEM image of S-C<sub>2</sub>N<sub>4</sub>, (f) TEM images of the S-C<sub>2</sub>N<sub>4</sub> (inset shows the HRTEM image), and (g) atomic-resolution inverted STM image of S-C<sub>2</sub>N<sub>4</sub> on Cu (111). Inset shows the superimposition of the S-C<sub>2</sub>N<sub>4</sub> structure (left), atom positions (top-right), and the topographic height profile along the dark red line (down-right). (h) N<sub>2</sub> adsorption–desorption isotherms of C<sub>3</sub>N<sub>4</sub>, C<sub>2</sub>N<sub>4</sub>, P-C<sub>2</sub>N<sub>4</sub>, and S-C<sub>2</sub>N<sub>4</sub>. Reprinted with permission from ref. 19 copyright 2017 American Chemical Society.

confirms the holey C<sub>2</sub>N structure of the nanoribbons in aerogels and the inter-hole spacing is measured to be  $\sim 8.27 \pm 1$  Å (Fig. 4g), agreeing with the calculated studies.<sup>20</sup> Remarkably, the SSAs of S-C<sub>2</sub>N<sub>4</sub> (1943 m<sup>2</sup> g<sup>-1</sup>), P-C<sub>2</sub>N<sub>4</sub> (1468 m<sup>2</sup> g<sup>-1</sup>) and C<sub>2</sub>N<sub>4</sub> (1145 m<sup>2</sup> g<sup>-1</sup>) are much higher than that of the C<sub>2</sub>N crystals prepared by Baek *et al.* (26 m<sup>2</sup> g<sup>-1</sup>) (Fig. 4h).

As is known, good control over chemical reactions is highly important for tuning the local elemental distribution and structure at the atomic level of nanomaterials. In this context, Fechner and co-workers<sup>24</sup> proposed a eutectic synthesis approach using precursors containing pre-organized nitrogen atoms to realize a controlled polycondensation process instead of a spontaneous process for achieving 2D C<sub>2</sub>N nanocrystals (Fig. 5a–c). A supramolecular pre-organized mixture of cyclohexanehexone and urea was adopted as precursors, in which the former served as the structure donating motif and the latter could reduce the melting point of the mixture and also provided a nitrogen source. Through a controlled condensation–polymerization reaction and a carbonization process at suitable temperature, graphene-like 2D C<sub>2</sub>N with a stoichiometric ratio of 2 : 1 was fabricated. Based on this approach, other pre-organized precursors were also employed to synthesize graphene-like C<sub>2</sub>N with a stoichiometric C/N ratio of 2 : 1, but yet disordered. For instance, Jordan *et al.*<sup>25</sup> successfully

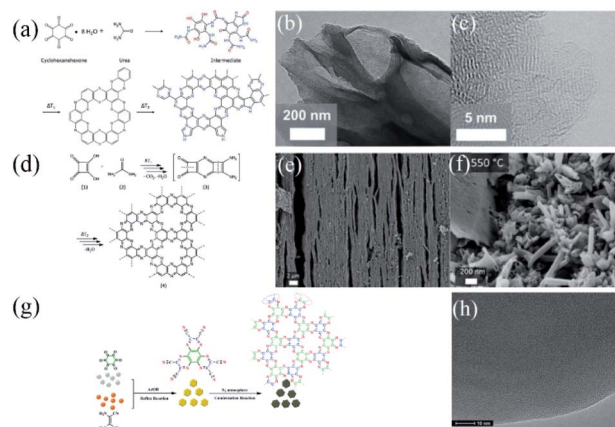


Fig. 5 (a) Reaction process scheme of C<sub>2</sub>N by Fechner *et al.* (cyclohexanehexone reacted with urea reactants to produce a cross-linked intermediate, which was then converted stepwise to nitrogen functionalized carbons containing primarily pyridinic and pyrazinic nitrogens at temperatures above 500 °C ( $T_1 < T_2$ )) and (b) SEM and (c) TEM images of the resultant product. (a–c) Reprinted with permission from ref. 24 copyright 2015 Wiley-VCH Verlag GmbH & Co. KGaA, Weinheim. (d) Reaction process scheme of C<sub>2</sub>N by Jordan *et al.* (squaric acid (1) reacted with urea (2), heated to form squaramide (3) by transamidation and squaramide was then converted into a C<sub>2</sub>N material (4) via condensation and ring rearrangement at elevated temperature ( $T_1 < T_2$ )). (e and f) SEM images of the primary supramolecular crystals formed from squaric acid (SA) and urea (U) in a ratio of (a and c) 1 : 1 (SA/U-1) and (b and d) 1 : 2 (SA/U-2), respectively. The two kinds of complex were treated after thermal condensation of 550 °C. (d–f) Reprinted with permission from ref. 25 copyright 2016 Curtin University of Technology and John Wiley & Sons, Ltd. (g) Reaction progress of porous CN materials by Li *et al.* (h) TEM image of the resultant product. (g and h) Reprinted with permission from ref. 26 copyright 2019 Elsevier Ltd.

prepared laminar C<sub>2</sub>N crystals starting from squaric acid and urea (Fig. 5d–f). Recently, Walczak *et al.*<sup>9b</sup> and Li *et al.*<sup>26</sup> reported the synthesis of porous C<sub>2</sub>N materials (SSA > 600 m<sup>2</sup> g<sup>-1</sup>) via carbonizing a hexaazatriphenylene precursor at 550 °C while the resultant C<sub>2</sub>N (C-HAT-CN-550) was rather thick and disorganized (Fig. 5g and h).

C<sub>2</sub>N can be prepared by wet-chemical methods<sup>9a,19</sup> and solid phase methods.<sup>9b,24–26</sup> Compared to the solid phase method, the synthetic procedure of the wet-chemical method is more complex, and the reaction process of the wet-chemical method is more difficult to control. In addition, with different precursors and reaction conditions, the synthesized C<sub>2</sub>N can have different morphologies, including nanosheets,<sup>13</sup> aerogels,<sup>27</sup> zeolite-like,<sup>26</sup> shale-like and hollow-tube.<sup>25</sup> Accordingly, these products possess distinct structural characteristics and physicochemical properties with respect to SSA, defective level, carrier mobility, *etc.*, which enable them to be applied in different fields.

### 2.3 Electronic properties of C<sub>2</sub>N

Baek *et al.* examined the electronic properties of C<sub>2</sub>N-h2D crystals by fabricating C<sub>2</sub>N-h2D-based FET devices.<sup>9a</sup> The semiconducting character of C<sub>2</sub>N-h2D crystals was validated and

a maximum on/off current ratio of  $4.6 \times 10^7$  was observed with the electron mobility and hole mobility of  $13.5 \text{ cm}^2 \text{ V}^{-1} \text{ s}^{-1}$  and  $20.6 \text{ cm}^2 \text{ V}^{-1} \text{ s}^{-1}$ , respectively. Moreover, the bandgap was determined to be 1.96 eV, which is close to the value derived from DFT calculations (1.70 eV). Compared to g- $\text{C}_3\text{N}_4$  (2.7 eV),<sup>15a</sup> the narrower bandgap of  $\text{C}_2\text{N}$ -h2D crystals provides them with better visible light absorption, which is beneficial to their photocatalytic applications. Similar to other 2D semiconducting materials, the bandgap of  $\text{C}_2\text{N}$  also varies with the crystal thickness. Unfortunately, most of the relevant research studies are theoretically conducted without support from experimental evidence. For instance, Zhang *et al.* performed a first principles study on the electronic properties of few-layer  $\text{C}_2\text{N}$ -h2D crystals with DFT calculations.<sup>35</sup> The authors reported that the band structure, especially splitting of the bands, and bandgap of this system depend on the stacking order between the layers, whereas the bandgap exhibits a monotonically decreasing behavior as the layer number increases. A recent theoretical study suggested that the direct bandgap of  $\text{C}_2\text{N}$ -h2D can be decreased by 34% with the evolution of structure from monolayer to bulk.<sup>36</sup> Therefore, these studies offer a strategy to modulate the bandgap of  $\text{C}_2\text{N}$  from the near-infrared to green visible wavelength by controlling the stacking order and layer number of the crystal.

The electronic properties of  $\text{C}_2\text{N}$  can also be modulated by doping with metal and non-metal elements (*e.g.* Fe, Co, Ga, Au, F, Cl, Si, Ge, P and As)<sup>27–30</sup> based on diverse computational studies. For example, Ma *et al.*<sup>34</sup> theoretically investigated the atomic configurations and electrical properties of  $\text{C}_2\text{N}$  monolayers embedded with a single atom of V, Cr and Mn. The local-density-of-states indicated that all three composites show a non-bandgap feature, similar to that of conductors. Du *et al.*<sup>30</sup> reported that the Fermi level of  $\text{C}_2\text{N}$  increased and the bandgap decreased with the increase of P/As doping concentration.

Additionally, combining  $\text{C}_2\text{N}$  with another semiconductor (*e.g.* GaTe,<sup>31</sup>  $\text{C}_3\text{B}$ ,<sup>32</sup> g- $\text{C}_3\text{N}_4$ ,<sup>33</sup> BCN<sup>38</sup>) to construct a heterojunction is also a feasible option to modulate the electronic properties of  $\text{C}_2\text{N}$ . For example, the bandgap of  $\text{C}_2\text{N}$  can be tuned from direct to indirect by forming a monolayer  $\text{C}_2\text{N}/\text{GaTe}$  heterostructure, as suggested by the calculation results of Bai *et al.*<sup>31</sup> Moreover, the recombination of charge carriers in  $\text{C}_2\text{N}$  can be suppressed due to the formation of a built-in electric field in the heterojunction, which is desirable for its applications in optoelectronic devices and photocatalysis.

In summary, engineering the electronic properties of  $\text{C}_2\text{N}$  can be realized by thickness control, elemental doping and construction of heterostructures. For elemental doping, both the metal and non-metal dopants can modify the Fermi level and reduce the bandgap of  $\text{C}_2\text{N}$ , while the metal doping can significantly narrow the bandgap even down to zero, which makes the metal-doped  $\text{C}_2\text{N}$  not suitable for photocatalysis but as an electrocatalyst. Non-metal doping and constructing heterojunctions are effective strategies to modulate the band structure of  $\text{C}_2\text{N}$  while maintaining its semiconducting nature. Especially for heterostructured  $\text{C}_2\text{N}$ -based composites, both the light absorption and electron-hole pair separation efficiency are improved, making them appealing photocatalysts. The current

theoretical progress on the electronic properties of  $\text{C}_2\text{N}$  has guiding significance for promoting its practical applications in areas like electronics, catalysis, and photocatalysis.

## 2.4 Applications of $\text{C}_2\text{N}$

With the intrinsic semiconducting properties and tunable electronic structure,  $\text{C}_2\text{N}$  holds great potential in photocatalysis. Therefore, many studies have demonstrated the photocatalytic performance of  $\text{C}_2\text{N}$  and  $\text{C}_2\text{N}$ -based materials in different reactions. Meanwhile, the 2D planar and nanoporous structure of  $\text{C}_2\text{N}$  make it an outstanding support for loading metal atoms to obtain metal@ $\text{C}_2\text{N}$  composite catalysts for various reactions. Especially, the edge N atoms in the nanopores of  $\text{C}_2\text{N}$  can effectively trap metal atoms, promoting the bonding between the metals and support. Furthermore, the nanoporosity of  $\text{C}_2\text{N}$  also makes it an efficient adsorbent for various gases. Overall, an increasing interest has been focused on the applications of  $\text{C}_2\text{N}$ -based materials in different areas.

**2.4.1 Photocatalysts.** As a semiconductor, the suitable bandgap of  $\text{C}_2\text{N}$  also enables it to serve as a promising visible light-activated photocatalyst. Zhang and Yang theoretically assessed the photocatalytic performances of 2D  $\text{C}_2\text{N}$  with different layers (1–5 layers) for water splitting.<sup>37</sup> Their calculations suggested that these few-layer  $\text{C}_2\text{N}$  nanocrystals have a good response to visible light and may serve as potential nonmetal photocatalysts for water splitting, while bilayer  $\text{C}_2\text{N}$  is the most promising one. Furthermore, heterostructured  $\text{C}_2\text{N}$  composite photocatalysts are proposed aiming at enhancing the photocatalytic activity of  $\text{C}_2\text{N}$ .<sup>38</sup> For instance, modelling of van der Waals heterostructures of BCN/ $\text{C}_2\text{N}$  and  $\text{C}_3\text{N}_4/\text{C}_2\text{N}$  was conducted by Zhang *et al.*<sup>38</sup> and Yang *et al.*,<sup>33</sup> respectively. The two studies both revealed that the photocatalytic activity of  $\text{C}_2\text{N}$  for water splitting is enhanced by constructing heterostructures due to the increased separation efficiency of charge carriers. Unfortunately, relevant experimental studies have barely been reported in the literature.

**2.4.2 Catalyst support of electrochemical catalysis for water splitting.** In light of the 2D planar structure and high SSA of  $\text{C}_2\text{N}$ , it is also considered as a suitable support for loading metals to synthesize heterogeneous catalysts for various reactions. Particularly, the N atoms in the aromatic rings of  $\text{C}_2\text{N}$  can serve as anchoring sites for metal atoms. Baek and co-workers investigated the catalytic activity of a cobalt nanoparticle-doped  $\text{C}_2\text{N}$  composite ( $\text{Co}@C_2N$ ) for the hydrogen evolution reaction (HER) in alkaline sodium borohydride solution and observed that such a catalyst exhibited a better reactivity than the reported noble metal catalysts.<sup>23</sup> The authors stated that the enhanced catalytic activity and good stability originate from the strong interaction between the metallic nanoparticles and the substrate. In another study, they compared the HER performances of a diversity of metal nanoparticle-doped  $\text{C}_2\text{N}$  composites ( $\text{Co}@C_2N$ ,  $\text{Ru}@C_2N$ ,  $\text{Ni}@C_2N$ ,  $\text{Pd}@C_2N$  and  $\text{Pt}@C_2N$ ).<sup>40</sup>  $\text{Ru}@C_2N$  outperformed the other four composites as well as the typical Pt/C catalyst in both acidic and alkaline solutions. S- $\text{C}_2\text{N}$ A was also demonstrated to possess excellent catalytic activities in both oxygen evolution reaction (OER) and

oxygen reduction reaction,<sup>19</sup> deriving from its high SSA and a high proportion of pyridinic plus graphitic N catalytic sites in the total N atoms (55%). With the superior bifunctional performance, the Zn-air and Li-O<sub>2</sub> batteries based on the S-C<sub>2</sub>NA electrode show high efficiency in energy conversion and storage. Additionally, the HER and OER activities of C<sub>2</sub>N supported SACs (metal<sub>1</sub>@C<sub>2</sub>N) are also assessed by calculating the overpotential with first principles computations.<sup>38,41</sup> Zhang's group conducted a systematic study on the catalytic properties of a wide range of C<sub>2</sub>N supported transition metal (TM) catalysts (TM<sub>1</sub>@C<sub>2</sub>N).<sup>42</sup> The pure C<sub>2</sub>N was discovered to be inactive for the HER due to the strong bonding between H<sub>2</sub> and N atoms, but the doping with TMs significantly modified the catalytic activity. By comparison, Ti<sub>1</sub>@C<sub>2</sub>N manifested the best HER activity but poor OER activity, whereas Mn<sub>1</sub>@C<sub>2</sub>N was found to be a suitable bifunctional electrocatalyst for both HER and OER because it exhibited an overpotential of only 0.67 V in OER and the Gibbs free energy changes for H<sub>2</sub> adsorption on Mn<sub>1</sub>@C<sub>2</sub>N were slightly above zero.

**2.4.3 Catalyst support for CO oxidation.** The catalytic activity of C<sub>2</sub>N supported metal catalysts in CO oxidation has also been investigated, while the relevant studies are mainly performed by theoretical calculations.<sup>16b,34,39,43</sup> For instance, He *et al.*<sup>43a</sup> predicted the stable presence of a single Fe atom trapped in the cavity of a C<sub>2</sub>N monolayer by calculating the adsorption energy and diffusion barrier and demonstrated the excellent CO oxidation ability of the Fe-embedded C<sub>2</sub>N SAC at different temperatures. Ma *et al.*<sup>34</sup> used the first-principles calculation to study CO oxidation catalyzed by various 3d TM-embedded C<sub>2</sub>N SACs (TM = Sc, Ti, V, Cr, Mn, Fe, Co, Ni, Cu, Zn). Their results illustrated that C<sub>2</sub>N monolayers are promising substrates for 3d TM SACs, while Cr- and Mn-embedded C<sub>2</sub>N catalysts show the best catalytic CO oxidation performances. Recently, Li and Chen<sup>16b</sup> systemically investigated the reaction mechanism of CO oxidation and the gas adsorption with the single-atom and bi-atom catalysts of copper. The C<sub>2</sub>N embedded with a copper dimer (Cu<sub>2</sub>@C<sub>2</sub>N) catalyst was revealed to show a superior catalytic performance to the SAC (Cu<sub>1</sub>@C<sub>2</sub>N). Meanwhile, different mechanisms of CO oxidation by Cu<sub>1</sub>@C<sub>2</sub>N and Cu<sub>2</sub>@C<sub>2</sub>N were proposed. The Eley-Rideal mechanism is responsible for the Cu<sub>2</sub>@C<sub>2</sub>N-catalyzed CO oxidation rather than the Langmuir-Hinshelwood mechanism, which is contrary to the metal-doped (metal = Al, Sc, Ti, V, Cr, Mn, Fe, Co, Ni, Cu, Zn, *etc.*) graphene,<sup>44</sup> but similar to the Ni-embedded divacancy graphene.<sup>45</sup> A tri-molecular Eley-Rideal (T-E-R) mechanism accounts for the Cu<sub>1</sub>@C<sub>2</sub>N-catalyzed CO oxidation in which the adsorption of two CO molecules can assist the breaking of the O-O bond in O<sub>2</sub> (Fig. 6). Moreover, a doped C<sub>2</sub>N catalyst with oxygen was also proposed to be capable of improving the CO oxidation performance due to the extra electrons brought by oxygen.<sup>39</sup>

**2.4.4 Catalyst supports for the CO<sub>2</sub> reduction reaction (CO<sub>2</sub>RR) and nitrogen reduction reaction (NRR).** C<sub>2</sub>N supported metals have also been verified to be efficient catalysts for the CO<sub>2</sub>RR and NRR. For example, Cui *et al.*<sup>27</sup> tested the CO<sub>2</sub>RR activity of twelve types of SACs supported by C<sub>2</sub>N through calculations. The results implied that the product selectivity

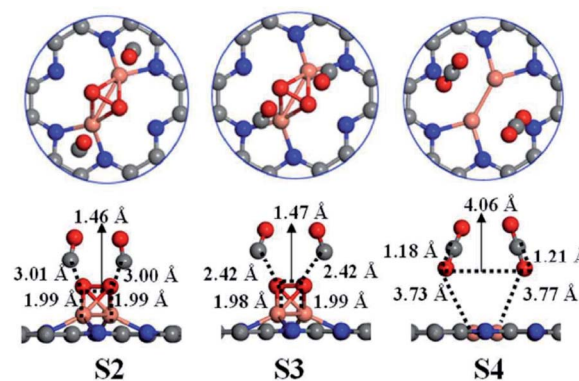


Fig. 6 Atomic configurations of S2–S4 and the key structural parameters for CO oxidation via the T-E-R mechanism on Cu<sub>2</sub>@C<sub>2</sub>N. Color scheme: C, gray; N, blue; O, red; Cu, orange. Reprinted with permission from ref. 16b, copyright 2018 The Royal Society of Chemistry.

(methane or methanol) can be tuned by changing the embedded metal atom species. The CO<sub>2</sub> electro-reduction performances of Cu<sub>1</sub>@C<sub>2</sub>N and Cu<sub>2</sub>@C<sub>2</sub>N as reported by Zhao *et al.*<sup>46</sup> were also compared and the former was still inferior to the latter. Wang *et al.*<sup>47</sup> firstly reported that Mo@C<sub>2</sub>N shows a low onset potential of -0.17 V in NRR via DFT calculations, indicating that it may be a low-cost and high-efficient catalyst for electrochemical conversion of N<sub>2</sub> to NH<sub>3</sub>. Recently, Zhou's group performed a systematic investigation on the NRR activity of nine C<sub>2</sub>N supported TM SACs or bi-atom catalysts.<sup>48</sup> This comprehensive study predicted that the Mo bi-atom catalyst supported by C<sub>2</sub>N is the most suitable one for the NRR.

**2.4.5 Other applications.** Apart from catalyst support, the uniformly distributed pores, special pore size and outstanding chemical stability of C<sub>2</sub>N make it a good candidate for membrane materials for gas separation, H<sub>2</sub> storage, CO<sub>2</sub> adsorption, seawater pervaporation and volatile organic compound (VOC) adsorption.<sup>49</sup>

The width of the pores in C<sub>2</sub>N is estimated to be 3.0 Å, smaller than that of O<sub>2</sub>, N<sub>2</sub>, CO, and CO<sub>2</sub>, but larger than the kinetic diameter of H<sub>2</sub> (2.89 Å) and He (2.6 Å).<sup>49f</sup> Thus, C<sub>2</sub>N may serve as a promising H<sub>2</sub> and He gas separation membrane material. In addition, the unique porous structure of C<sub>2</sub>N also makes it a potential adsorbent for gases like H<sub>2</sub>, CO<sub>2</sub> and VOCs. Hashmi *et al.*<sup>49b</sup> explored the H<sub>2</sub> adsorption of C<sub>2</sub>N and Li decorated C<sub>2</sub>N using the DFT method, and found that the Li decoration significantly improved H<sub>2</sub> adsorption on C<sub>2</sub>N. A theoretical gravimetric density of 13 wt% was reached for Li decorated C<sub>2</sub>N, which is much higher than that reported for other 2D materials decorated with alkali metals. Walczak and co-workers<sup>49d</sup> reported that CO<sub>2</sub> adsorption uptake of the prepared C<sub>2</sub>N sample (C-HAT-CN-550) reached a high value of 3.24 mmol g<sup>-1</sup> (at 273 K and *p* = 0.15 bar). Lu's group<sup>28</sup> theoretically studied CO<sub>2</sub> capture properties on metal-embedded C<sub>2</sub>N. Incorporation of open metal sites into the C<sub>2</sub>N framework can enhance the bonding of CO<sub>2</sub> on the adsorbent along with low-temperature desorption capacity. The authors screened a series of metal-embedded C<sub>2</sub>N including Ca and the

early 3d TMs as CO<sub>2</sub> adsorbents and found that Ca-embedded C<sub>2</sub>N shows the most promising reversible CO<sub>2</sub> capture performance. From DFT calculations, Ao *et al.*<sup>49c</sup> found that pure C<sub>2</sub>N can adsorb some typical VOCs like formaldehyde, benzene and trichloroethylene. Moreover, the adsorption ability of C<sub>2</sub>N can be improved by Al doping. In their later study, the Al-doped C<sub>2</sub>N was found to co-adsorb H<sub>2</sub>O and O<sub>2</sub>, implying the possible generation of hydroxyl and superoxide radicals, showing promising applications for VOC degradation as the hydroxyl and superoxide radicals are highly oxidizing species.<sup>50</sup>

Besides the aforementioned applications, Xu and co-workers also applied C<sub>2</sub>N as an electrode material for lithium-ion batteries (LIBs) and a high initial discharge capacity and high stability of C<sub>2</sub>N-based LIBs were observed.<sup>13a</sup>

### 2.5 Summary of C<sub>2</sub>N

Thanks to the efforts of Baek and co-workers, the 2D C<sub>2</sub>N crystal has attracted wide attention in the last five years, due to its high stability, hole structure, high SSA, and other physical and chemical properties. Although there are several methods to synthesize C<sub>2</sub>N, the complex synthesis process and the expensive and rare precursors limit its large-scale production and practical applications. Therefore, it is urgent to develop low-cost and easy-operation methods to fabricate the 2D C<sub>2</sub>N crystal. As a kind of semiconductor, the 2D C<sub>2</sub>N crystal has a tunable bandgap, high carrier mobility, and special porous structure, which enable it to perform well in areas like FET,<sup>9a</sup> HER<sup>23</sup> and LIBs.<sup>13a</sup> In addition, based on DFT calculations, researchers reported the promising use of 2D C<sub>2</sub>N materials in the OER,<sup>42</sup> CO oxidation,<sup>34</sup> CO<sub>2</sub>RR,<sup>27</sup> NRR,<sup>48</sup> and gas adsorption.<sup>49</sup> Moreover, Mahmood *et al.*<sup>9a</sup> predicted that C<sub>2</sub>N could be used in electrodes for energy storage, gas storage and some other areas. The applications of C<sub>2</sub>N are summarized in Fig. 7.

## 3. C<sub>3</sub>N

The possible crystal structure of 2D C<sub>3</sub>N was predicted as an indirect-bandgap semiconductor a few decades ago and it aroused much interest from the scientific community.<sup>51</sup> Therefore, a considerable amount of effort on its synthesis was attempted, but to achieve amorphous products in a C<sub>3</sub>N stoichiometry without a 2D structure, which could not testify the

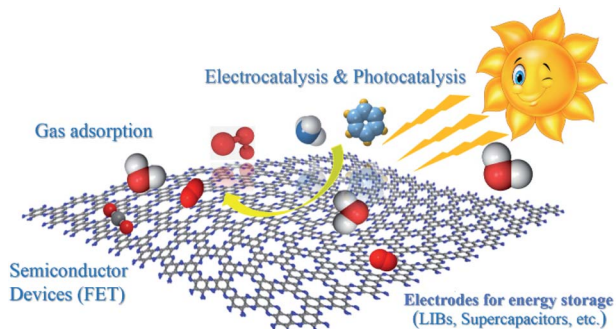


Fig. 7 Potential applications of the C<sub>2</sub>N-h2D crystals.

theoretical calculations.<sup>52</sup> Until 2016, Baek and co-workers<sup>13a,53</sup> successfully synthesized a 2D layered C<sub>3</sub>N nanocrystal, whose structure was in good agreement with the predictions. Then, this new member of the 2D C<sub>x</sub>N<sub>y</sub> family has been widely applied as a catalyst, electrode material, and adsorbent, due to its peculiar electrical and chemical properties.

### 3.1 Crystalline Structure of C<sub>3</sub>N

A C<sub>3</sub>N monolayer can be regarded as a N-doped graphene structure, where the molar ratio of C to N is 3 : 1 and all the N atoms belong to graphitic N. Similar to graphene, the atoms in C<sub>3</sub>N also exhibit sp<sup>2</sup> hybridization.<sup>54</sup> Apparently, the C<sub>3</sub>N framework is quite different from the C<sub>2</sub>N framework, where periodic holes are not included. The monolayer C<sub>3</sub>N has a lattice parameter of 4.863 Å, with the C–N bond length of 1.403 Å and the C–C bond length of 1.404 Å.

### 3.2 Synthesis of C<sub>3</sub>N

Compared to C<sub>2</sub>N, there are less available methods for the synthesis of C<sub>3</sub>N. King *et al.*<sup>55</sup> obtained a mixture of amorphous C<sub>3</sub>N flakes with a thickness of 1–3 μm and graphitic carbon microspheres through annealing a nitrogen-rich polymer precursor (*m*-phenylenediamine) in a vacuum-sealed quartz

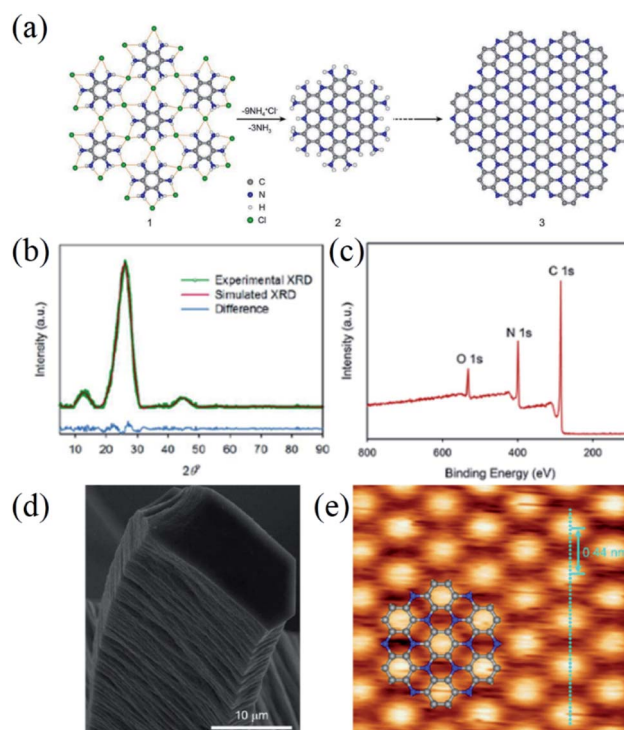


Fig. 8 (a) Schematic representation of C<sub>3</sub>N, (b) experimental PXRD pattern from C<sub>3</sub>N (dark green), simulated XRD after Pawley refinement (dark red) and the difference (dark blue), (c) XPS survey spectrum of C<sub>3</sub>N, (d) SEM image of C<sub>3</sub>N, and (e) STM image of a 2D PANI framework (2.5 × 2.5 nm<sup>2</sup>, V<sub>s</sub> = −1.1 V, I<sub>t</sub> = 1.0 nA). Inset structure represents C<sub>3</sub>N repeating units with carbon atoms (gray balls) and nitrogen atoms (blue balls). Reprinted with permission from ref. 53 copyright 2016 National Academy of Sciences.

tube at 800 °C for 7–9 days. To improve the crystallinity of  $C_3N$ , Baek and co-workers<sup>13a,53</sup> then used organic hexaaminobenzene trihydrochloride (HAB,  $C_6N_6H_{15}Cl_3$ ) crystals as precursors and successfully obtained 2D layered  $C_3N$  nanocrystals by decomposing the HAB into  $C_6N_2$ ,  $NH_4Cl$ , and  $NH_3$  at 500 °C for 2 h under an argon atmosphere (Fig. 8a). The resultant  $C_3N$  nanocrystal is multilayered and represents a similar hexagonal morphology to the HAB crystals.<sup>53</sup> The interlayer distance of the as-prepared  $C_3N$  nanocrystal is estimated to be 3.40 Å according to the XRD characteristic peak at  $2\theta$  of 26.12° (Fig. 8b). In addition, another two major peaks at  $2\theta$  of 12.8° and 44.7° are also present in the XRD pattern. Meanwhile, the authors confirmed the  $C_3N$  chemical composition, molecular structure and bond nature of the as-prepared nanocrystal *via* XPS (Fig. 8c).<sup>53</sup> Furthermore, the 2D  $C_3N$  framework at the atomic level was unambiguously illustrated with the assistance of the STM method and the dot-to-dot distance in the well-ordered triangular structure of  $C_3N$  was found to be  $442 \pm 16$  pm, which was in good match with the DFT modelling (Fig. 8e).

Recently, fabrication of  $C_3N$  quantum dots (QDs) was reported by Yang *et al.*<sup>13b</sup> In their work, a precursor of 2,3-diaminophenazine (DAP) is polymerized by a typical hydrothermal method, forming  $C_3N$  QDs and  $C_3N$  nanosheets (Fig. 9a). The layered  $C_3N$  was formed at a DAP concentration of 0.8 mM and 250 °C. Especially, by prolonging the polymerization reaction time to 200 h, 2D  $C_3N$  nanocrystals containing a high proportion of large, single-layer and single crystalline nanosheets can be obtained (Fig. 9b and c). For QDs, the size can be controlled in the range of 1.8–5.5 nm by varying the concentration of DAP solution and hydrothermal temperature (Fig. 9d and e).

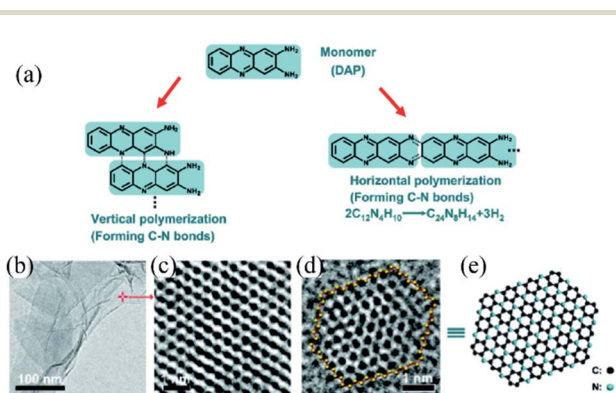


Fig. 9 (a) Schematic of the vertical and horizontal polymerization of DAP forming C–N bonds. The polymerization advances *via* abstraction of H from C–H and N–H bonds followed by formation of C–N bonds. (b) TEM image of a mixture of single- and multilayer  $C_3N$  sheets, (c) spherical aberration-corrected HRTEM image showing the honeycomb structure of a single-layer sheet marked in (b), and (d) spherical aberration-corrected HRTEM image of a single  $C_3N$  QD with a C–N zigzag edged structure. The yellow balls represent the carbon and nitrogen atoms on the edge, while the red sticks represent the chemical bonds between atoms on the edge. (e) The molecular structure scheme of the  $C_3N$  QD in (d). Reprinted with permission from ref. 13b copyright 2017 Wiley-VCH Verlag GmbH & Co. KGaA, Weinheim.

### 3.3 Electronic properties of $C_3N$

$C_3N$  is an indirect bandgap semiconductor with the valence and conduction bands located at the  $M$  and  $\Gamma$  points, respectively.<sup>56</sup> Determination of the theoretical bandgap of a  $C_3N$  monolayer is still debatable since different computation software gives discrepant values while convincing experimental evidence is not available thus far.<sup>51b,54</sup> For instance, Zhou *et al.*<sup>56a</sup> derived a bandgap of 1.04 and 0.39 eV for a  $C_3N$  monolayer by using HSE06 software and the generalized gradient approximation (GGA) method, respectively.

Experimentally, Mahmood *et al.*<sup>53</sup> measured the bandgap of an as-prepared 2D  $C_3N$  framework to be 2.67 eV by using a lock-in detection technique with scanning tunnelling spectroscopy and electrochemical methods. This result is far away from the theoretical value, possibly because the thickness can affect the bandgap of  $C_3N$  nanocrystals. Surprisingly, Mahmood and co-workers found that doping the as-prepared multilayered  $C_3N$  with HCl could remarkably reduce its bandgap since the conductivity was improved from  $0.72 \pm 0.04$  S  $cm^{-1}$  (undoped) to  $1.41 \times 10^3$  S  $cm^{-1}$  (doped). In fact, the HCl-doped 2D  $C_3N$  almost behaves as a conductor, which is more coincident with the calculations.

Yang *et al.*<sup>13b</sup> measured the bandgap of  $C_3N$  QDs based on ultraviolet photoelectron spectroscopy and UV-vis spectroscopy. It was found that the bandgap value of  $C_3N$  QDs decreases with increasing diameters of the QDs, *e.g.*, the bandgap varies from 2.74 to 0.39 eV with the size of QDs ranging from 1.8 to 30 nm. A further increase of the QD size larger than 30 nm barely affects the bandgap. Such a feature of size-dependent bandgaps provides  $C_3N$  QDs with tunable photoluminescence, favoring their applications in bioimaging. Notably, the unique bandgap structure of  $C_3N$  QDs also enables them to have a much higher quantum yield and life-time than graphene QDs. In addition, Yang *et al.*<sup>13b</sup> also investigated the electrical properties of a monolayer  $C_3N$  nanosheet with FET devices. The average  $I_{ON}/I_{OFF}$  ratio for the  $C_3N$ -based FETs reached  $5.5 \times 10^{10}$  and the hole and electron mobilities of the  $C_3N$  monolayer were measured to be 1.2 and 1.5  $cm^2 V^{-1} s^{-1}$  respectively. Notably, the  $I_{ON}/I_{OFF}$  ratio of  $C_3N$  is three orders of magnitude higher while the carrier mobility is lower than that of  $C_2N$ -h2D crystals. Interestingly, theoretical calculations reported that the carrier mobility of  $C_3N$  is anisotropic and the hole mobility along the armchair direction of the  $C_3N$  monolayer can reach up to  $1.08 \times 10^4$   $cm^2 V^{-1} s^{-1}$ , much higher than that of  $C_2N$ -h2D crystals.<sup>56b</sup> These results demonstrate that the intrinsic conductivity and carrier mobility of  $C_3N$  are better than those of  $C_2N$ , indicative of the promising applications of  $C_3N$  in FET devices and electrode materials. The hole and electron mobility of  $C_3N$  could be further improved to 180 and 220  $cm^2 V^{-1} s^{-1}$ , respectively, by hydrogenation in  $H_2$ , while the intrinsic mechanism is unknown yet. Interestingly, the hydrogenated  $C_3N$  nanosheet even exhibits a ferromagnetic state according to both the DFT calculations and magnetic performance measurements.

Several theoretical studies demonstrated that the electronic properties of  $C_3N$  can also be modulated by forming heterojunctions with another semiconductor (*e.g.*  $g-C_3N_4$ ,<sup>57</sup>  $C_3B^58$ ).

Due to the narrow bandgap and good carrier mobility of  $C_3N$ , it can act as a photosensitizer to enhance the visible light absorption and also retard the charge recombination of the heterostructure, which can improve the photocatalytic activity.

### 3.4 Application of $C_3N$

As a semiconductor with a small bandgap,  $C_3N$  shows a broad-band solar light absorption, which indicates its potential utilization in photocatalysis. Meanwhile, because of the structural similarity to N-doped graphene which exhibits good electrocatalytic activities for reactions like the ORR, HER, *etc.*, the potential application of  $C_3N$  in electrocatalysis was investigated. Furthermore,  $C_3N$  is also considered as a promising electrode material for batteries and as a gas adsorbent owing to its peculiar electrical properties and planar structure. The applications of  $C_3N$  in photocatalysis, electrocatalysis, batteries and gas adsorption are summarized in this section.

**3.4.1 Photocatalysts.** Due to the wide spectral responsive range and high carrier mobility,  $C_3N$  is typically combined with other semiconductors to construct heterostructured photocatalysts for enhanced photocatalytic performance. For instance, Wang *et al.*<sup>57</sup> designed  $C_3N/g-C_3N_4$  heterojunctions and evaluated their ability for photocatalytic water splitting *via* DFT calculations. The authors found that the strong interlayer interaction between  $C_3N$  and  $g-C_3N_4$  nanosheets drives the charge transfer in the heterojunction to follow a Z-scheme pathway, which significantly improves the carrier separation efficiency. Meanwhile, the integrated  $C_3N/g-C_3N_4$  system has a wider light absorption range from the ultraviolet to the near infrared region compared to the single  $g-C_3N_4$  system that hardly absorbs visible light. With the improved charge separation, stronger visible light absorption ability and suitable valence band position, the  $C_3N/g-C_3N_4$  heterojunction can serve as an excellent photocatalyst for overall water splitting under visible light irradiation. Very recently, Niu *et al.*<sup>58</sup> computationally demonstrated that the  $C_3B/C_3N$  heterojunction also functions as a promising metal-free direct Z-scheme photocatalyst for water splitting under visible light irradiation. Due to the p-type semiconducting feature of  $C_3B$  and n-type feature of  $C_3N$ , they interacted with each other intensely to result in the formation of a built-in electric field from  $C_3N$  to  $C_3B$  in the heterojunction, which remarkably retards the electron-hole recombination rate and promotes the redox ability of photoinduced charges (electrons and holes) for  $H_2O$  molecules. Additionally, the Lewis acid B atoms in the  $C_3B$  lattice were found to be capable of adsorbing  $H_2O$  molecules efficiently, which also benefits the photocatalytic water splitting reaction.

**3.4.2 Electrocatalysts.** Several theoretical studies have evaluated the electrocatalytic water splitting performance of  $C_3N$ -based catalysts.<sup>59</sup> Pristine  $C_3N$  is found to exhibit a poor electrocatalytic activity for water splitting, while chemical modifications of  $C_3N$  can significantly improve its catalytic properties. He *et al.*<sup>59b</sup> reported that the overpotential of B-doped  $C_3N$  in the ORR (0.6 V) was calculated to be slightly higher than that of the commonly used Pt electrocatalyst (0.45 V), indicating the comparable electrocatalytic activity of B-

doped  $C_3N$  to Pt for the ORR. The excellent electrocatalytic performance of B-doped  $C_3N$  is attributed to the reason that the electron-deficient B atoms can effectively adsorb  $O_2$  molecules and the B-N and B-C bonds are quite active towards the ORR. In addition, Xu *et al.*<sup>59a</sup> showed that the B-doped  $C_2N/C_3N$  coplanar heterojunction is a promising electrocatalyst for the HER because of the good electrical conductivity, accelerated charge transfer and the low Tafel barrier of 0.86 eV which favor the HER at room temperature. Recently, Zhou *et al.*<sup>59c</sup> studied the OER and ORR properties of the  $C_3N$  monolayer embedded with different types of metal atoms (Mn, Fe, Co, Ni, Rh, Pd, Ir and Pt) based on DFT calculations. All the metal-embedded  $C_3N$  monolayers exhibit metallic properties and the Rh-embedded  $C_3N$  shows the best OER and ORR activities with the overpotentials of 0.35 V and 0.27 V, respectively.

**3.4.3 Electrode materials for batteries.** Owing to the merits of large net positive charge densities, outstanding structural stability and enhanced electronic/ionic conductivity from the intrinsic 2D polyaniline framework of  $C_3N$ , this material is regarded as a promising alternative to graphite and graphene/carbon-based materials for the anode of metal ion batteries. Xu *et al.*<sup>13a</sup> evaluated the performance of a multilayered  $C_3N$  anode in LIBs and also made a comparison with  $C_2N$ , heat-treated  $C_2N$  at 450 °C ( $C_2N$ -450) and graphite (Fig. 10a). Interestingly,  $C_2N$ -450 manifests a higher reversible capacity but still lower rate capacity than  $C_2N$ , possibly because the heating treatment can improve the crystallinity, SSA and electrical conductivity of  $C_2N$ .  $C_3N$  displays a voltage hysteresis of 0.15 V (Fig. 10b) lower than that of  $C_2N$ -450 (Fig. 10c), which results from the lower SSA ( $C_3N$ : 54.4 m<sup>2</sup> g<sup>-1</sup>,  $C_2N$ -450: 280.5 m<sup>2</sup> g<sup>-1</sup>)

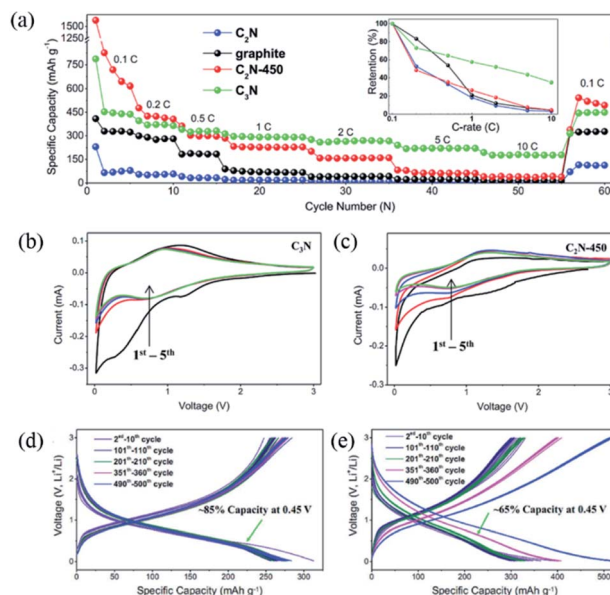


Fig. 10 (a) Rate capability measurements for  $C_2N$ ,  $C_2N$ -450,  $C_3N$ , and graphite at various C-rates from 0.1 to 10C. Representative cyclic voltammograms of (b)  $C_3N$  and (c)  $C_2N$ -450 for the five cycles at a scan rate of 0.1 mV s<sup>-1</sup>. Charge/discharge profiles of (d)  $C_3N$  and (e)  $C_2N$ -450 at 1C. Reprinted with permission from ref. 13a copyright 2017 Wiley-VCH Verlag GmbH & Co. KGaA, Weinheim.

and higher electrical conductivity. Furthermore,  $C_3N$  showed better cycling stability and a more efficient operating voltage window (nearly 85% of full discharge capacity secured at above 0.45 V) than  $C_2N$ -450 (nearly 65% of full discharge capacity secured at above 0.45 V) (Fig. 10d and e). Therefore, in terms of capacity, voltage hysteresis, efficient operating voltage window and cycling stability, which are the key factors for practical applications of electrode materials in LIBs,  $C_3N$  is more promising than  $C_2N$ -450 as well as graphene.

In the above work,<sup>13a</sup> a significant capacity loss in the first several cycles was witnessed (Fig. 10a), which limits its application in LIBs. Liu and co-workers<sup>60</sup> performed first-principles simulations on the intercalation process of Li ions into  $C_3N$  and suggested that the behavior is a result of N excess  $C_3N$  ( $C_{2.67}N$ ) in Xu's experiment.<sup>13a</sup> With the N excess in the  $C_3N$  framework, N-doping and carbon-vacancy defects are present, which strengthen the intercalation of Li ions into  $C_{2.67}N$  and the energy barriers of the deintercalation process. It was proposed that  $C_{3.27}N$  maintained high reversible capacity in LIBs. Later, Preeti *et al.*<sup>61</sup> demonstrated that the  $C_3N$  monolayer also serves as a promising anode material for Na/K-ion batteries with a storage capacity of up to 1072 mA h  $g^{-1}$  *via* first-principles calculations.

**3.4.4 Gas adsorbent.** Graphene has been widely applied as an adsorbent for various gases due to its extraordinary surface-volume ratio.<sup>62</sup> As a graphene-like 2D material, the gas adsorption capacities of  $C_3N$  have also been widely studied.<sup>16a</sup> Particularly, the substitution of N atoms with C atoms not only breaks the chemical inertness of the graphene framework but also lowers the work function, which enables  $C_3N$  to probably show better chemical activity towards gas molecules. For instance, Ma *et al.*<sup>63</sup> simulated the adsorption configuration of a series of gas molecules involving  $NO_2$ ,  $NO$ ,  $CO_2$ , and  $CO$  onto a  $C_3N$  monolayer. Compared to graphene,<sup>64</sup> the adsorption energy and charge transfer between the four molecules and  $C_3N$  are significantly enhanced. Meanwhile, the calculations showed that weak chemical adsorption with a large adsorption energy of  $\sim 0.8$  eV occurred between  $NO_2$  and  $C_3N$ , while the adsorption between the other gas molecules and  $C_3N$  belongs to physisorption with a lower adsorption energy.

Gas adsorption capacities of the  $C_3N$  monolayer were found to be improved by doping with inorganic or metal elements. Pashangpour and Peyghan<sup>65</sup> assessed the adsorption of  $CO$  onto B-doped and Al-doped  $C_3N$  nanosheets by DFT calculations. The introduction of B dopants barely promoted the weak physisorption of  $CO$  onto the pristine  $C_3N$  nanosheet, whereas the Al doping significantly enhanced the interaction between  $CO$  and  $C_3N$  nanosheets. Moreover,  $CO$  adsorption onto the Al-doped  $C_3N$  nanosheet induces noticeable changes of electrical conductivity of the sheet. These findings implied the potential application of Al-doped  $C_3N$  nanosheets as both the  $CO$  adsorbent and sensors. Recently, several computational studies demonstrated the excellently reversible  $CO_2$  capture capacity on the negatively polarized  $C_3N$  monolayer.<sup>66</sup> It was shown that the negative polarization could turn the physisorption of  $CO_2$  into chemisorption. In addition, the negatively charged  $C_3N$  monolayer was a promising material to separate  $CO_2$  from the

mixtures of  $CO_2/N_2$ ,  $CO_2/H_2$ ,  $CO_2/CH_4$ , and  $CO_2/C_2H_2$ , and to separate  $C_2H_2$  from the mixtures of  $C_2H_2/CH_4$  and  $C_2H_2/H_2$  through manipulating the negative charge density.<sup>66b</sup>

Multilayered  $C_3N$  crystals are also reported to be highly efficient for gas adsorption,<sup>67</sup> similar to multilayered graphene.<sup>68</sup> Li *et al.*<sup>16a</sup> constructed a periodic 3D pore model containing two  $C_3N$  monolayers (denoted as  $C_3N$  pores) with a pore size of 0.75 nm (Fig. 11a) and showed that the  $C_3N$  pores manifest an extremely high  $CO_2$  adsorption capacity up to 3.99 mmol  $g^{-1}$  in air at 23 °C. Moreover, the  $C_3N$  pores show preferential adsorption of  $CO_2$  over  $CO$ ,  $H_2$ , and  $CH_4$  and the  $CO_2$  selectivity could be further boosted by regulating the size of  $C_3N$  pores from 0.75 to 0.65 nm (Fig. 11b–d). The high selectivities in  $CO_2/CO$ ,  $CO_2/H_2$ , and  $CO_2/CH_4$  are ascribed to the larger polarizability and quadrupole moment of  $CO_2$  molecules than the other three gas molecules, which enables stronger interaction between  $CO_2$  molecules and the  $C_3N$  surface. Furthermore, the strong interaction between  $CO_2$  molecules and the  $C_3N$  surface causes the  $CO_2$  adsorption to slightly decrease in the presence of water (3.80 mmol  $g^{-1}$ ). Recently, Ma *et al.*<sup>69</sup> used ZIF-8 and urea as precursors to synthesize  $C_3N$ -type N-rich carbon layers and applied them in methanol adsorption. A sample (CN950) with a SSA of 1496  $m^2 g^{-1}$  reached the highest methanol adsorption capacity of 13.2 mmol  $g^{-1}$ .

### 3.5 Summary of $C_3N$

$C_3N$  has a graphene-like crystalline structure, good chemical stability and an indirect bandgap, enabling plentiful applications in electronics, photocatalysis, electrocatalysis, energy storage devices, and gas adsorption. Multilayered  $C_3N$  can be synthesized *via* a carbonization process of precursors containing C and N, which is much simpler than that for  $C_2N$  layers. However, available methods for preparing single-layered or few-layered  $C_3N$  nanosheets and controllable modifications of  $C_3N$  are quite limited. Due to the much narrower bandgap than that

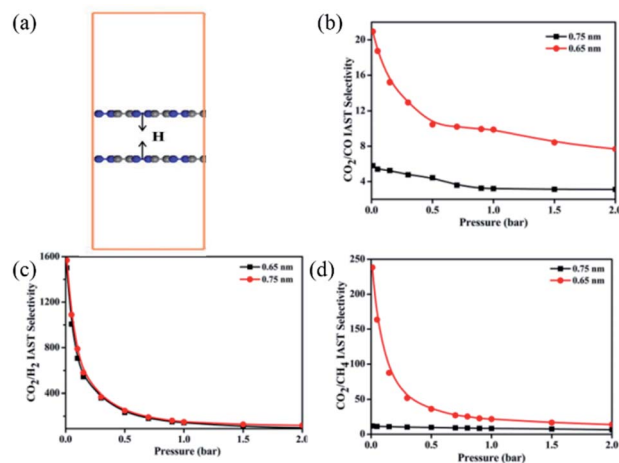


Fig. 11 (a) Molecular model of  $C_3N$  pores with a pore size of 0.75 nm. (b)  $CO_2/CO$ , (c)  $CO_2/H_2$ , and (d)  $CO_2/CH_4$  selectivity of  $C_3N$  pores with different pore sizes *versus* the adsorption pressure at 23 °C. Reprinted with permission from ref. 16a copyright 2017 American Chemical Society.

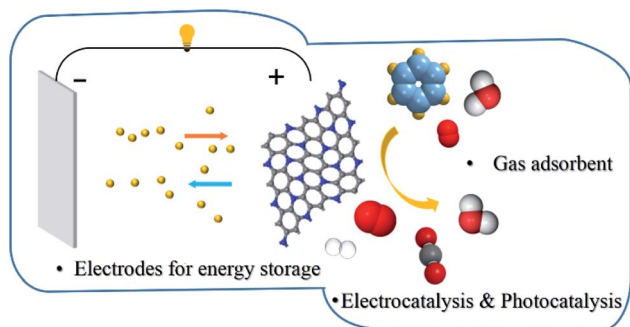


Fig. 12 Potential applications of  $C_3N$ .

of the  $C_2N$  monolayer, the  $C_3N$  monolayer itself possesses limited photocatalytic activity and it usually combines with other wide-bandgap semiconductors to form heterojunctions for photocatalysis. However, the better electrical conductivity and chemical stability of  $C_3N$  than  $C_2N$  enables it to have more promising applications in LIBs. In addition, the electrocatalytic activity of  $C_3N$  can be improved by rational chemical modifications. Furthermore, the gas adsorption capacity of  $C_3N$  can be tailored by doping, polarization and regulation of  $C_3N$  pores, making it a good candidate for a gas adsorbent. Definitely, the physicochemical and structural characteristics of  $C_3N$  are not fully understood thus far and there are still many potential applications for  $C_3N$  in the areas of environment and energy (as shown in Fig. 12). It is hoped that more efforts will be devoted to advance our knowledge in  $C_3N$ .

## 4 Graphite-like CN (g-CN)

The presence of g-CN nanocrystals has been reported for a long time, but little progress on its synthesis and applications has been made. In 2006, Cao *et al.*<sup>70</sup> proposed a simple solvothermal approach with cyanuric chloride and sodium precursors to obtain 1D CN nanostructures, which involves an initial formation of graphite-like carbon nitride (g-CN) layers followed by self-assembly into tubes, ribbons or microspheres (Fig. 13a–c). So far, the successful preparation of CN is absent in the literature. On the other hand, many theoretical studies have been conducted on the properties and potential applications of g-CN.

### 4.1 Crystalline structure of g-CN

The g-CN monolayer structure is composed of uniform holes and aromatic benzene rings containing three N atoms and three

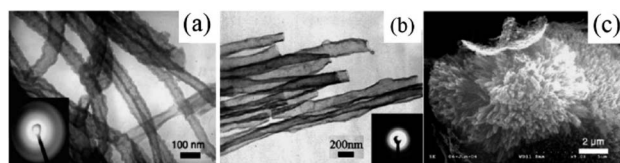


Fig. 13 (a) TEM image of a bundle of g-CN nanotubes and the embedded SAED, (b) TEM image of a bundle of g-CN nanoribbons (SAED embedded), and (c) SEM image of g-CN microspheres, reprinted with permission from ref. 70 copyright 2006 Elsevier Ltd.

C atoms alternatively arranged in the ring (Fig. 1).<sup>71</sup> The benzene rings are bridged by C–C bonds to form nanopores in g-CN, and all the N atoms belong to pyridine N. The lattice parameter is derived to be 7.12 Å, and the bond lengths of C–C and C–N are estimated to be 1.51 and 1.34 Å, respectively.

### 4.2 Electronic properties of g-CN

g-CN is predicted to behave as a semiconductor. To calculate the bandgap of the g-CN monolayer, Srinivasu *et al.*<sup>72</sup> used different methods and obtained different values. They stated that 2.89 eV should be more plausible based on Cao's work,<sup>70</sup> which observed broad photoluminescence peaks at 430–450 nm (corresponding to a bandgap of  $\sim 2.73$  eV) for the as-prepared g-CN nanotubes, nanoribbons and microspheres. Unluckily, experimental measurements in the bandgap of 2D g-CN crystals are unavailable yet. Meanwhile, Srinivasu *et al.*<sup>72b</sup> also studied the bandgap of multilayered g-CN and suggested that the bandgap decreased gradually from 2.89 to 2.72 eV with the layer number in the range of 1–6, which originates from the interlayer coupling. Furthermore, they found that doping the g-CN monolayer with phosphorus atoms (P@g-CN) could further reduce its bandgap to 2.31 eV, which corresponds to an appreciable visible light, whereas boron, oxygen and sulfur dopants are less efficient. Recently, Li *et al.*<sup>41</sup> reported that embedding a TM atom (TM = Pt, Pd, Co, Ni and Cu) into the g-CN framework could transform g-CN from a direct bandgap into an indirect bandgap with values of 0.41–0.52 eV. With the maneuverable band structure, g-CN is also expected to show great potential in photocatalysis.

### 4.3 Applications of g-CN

Unlike  $C_2N$  and  $C_3N$ , only a few examples of the applications of g-CN have been presented from computations in the literature. For instance, Srinivasu *et al.*<sup>72b</sup> evaluated the potential of g-CN, B@g-CN and P@g-CN for photocatalytic water splitting. P@g-CN is supposed to exhibit the best HER performance under visible light among the three samples due to its smaller bandgap, suitable conduction band minimum (CBM) position above the water oxidation potential and valence band minimum (VBM) position below the water reduction (Fig. 14a). In addition, the similar nanoporosity of g-CN to that of the  $C_2N$

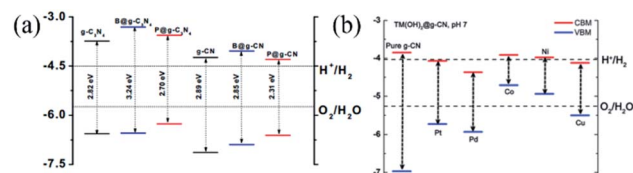


Fig. 14 (a) Calculated VBM and CBM positions of g- $C_3N_4$  and g-CN along with their boron and phosphorus doped counterparts, reprinted with permission from ref. 72b copyright 2014 American Chemical Society. (b) The energy band alignment of TM-(OH)<sub>2</sub>@CN. The vacuum level is set at 0 eV, and the chemical reaction potentials for  $H^+/H_2$  and  $O_2/H_2O$  are plotted with dotted lines. Reprinted with permission from ref. 41 copyright 2016 The Royal Society of Chemistry.

framework also makes it an excellent support of SACs for various reactions because the  $sp^2$ -hybridized N atoms at the vacancy hole edges can afford coordination sites to anchor the metal atoms. In this regard, Li *et al.*<sup>41</sup> designed a series of g-CN supported TM (TM = Pt, Pd, Co, Ni and Cu) SACs and studied their OER performances by DFT calculations (Fig. 14b). The computational results displayed that all the TM@g-CN materials function as good electrocatalysts for the OER and Co@g-CN is the most ideal one due to its lowest overpotential of  $\sim 0.16$  V. Although the TM@g-CN materials are not efficient to drive the water splitting under visible light irradiation due to their narrow bandgap (0.41–0.52 eV), the stable Pd-(OH)<sub>2</sub>@g-CN complex with modified band structure exhibits a promising photocatalytic activity for visible-light-driven OER. Recently, Chen *et al.*<sup>71</sup> demonstrated that a Li decorated g-CN monolayer presents a high efficiency in hydrogen storage systems, because of sufficient adsorption sites for hydrogen molecules. With the high Li loading, the Li decorated g-CN shows a good hydrogen adsorption performance with a theoretical gravimetric density of 10.81 wt%.

## 5. Other C<sub>x</sub>N<sub>y</sub>

Besides the aforementioned 2D C<sub>x</sub>N<sub>y</sub> structures, several other 2D C<sub>x</sub>N<sub>y</sub> compounds with different stoichiometries including C<sub>2</sub>N<sub>2</sub>, C<sub>2</sub>N<sub>3</sub>, C<sub>5</sub>N, and C<sub>5</sub>N<sub>2</sub> have also been reported in the literature, while less attention has been focused on them. Hence, we will give a brief introduction in this section.

### 5.1 Diamond-like CN (c-C<sub>2</sub>N<sub>2</sub>) and hexagonal CN (h-C<sub>2</sub>N<sub>2</sub>)

Recently, two new types of stable 2D C<sub>x</sub>N<sub>y</sub> were predicted by Dong *et al.*<sup>14</sup> via the DFT method, c-C<sub>2</sub>N<sub>2</sub> and h-C<sub>2</sub>N<sub>2</sub>. It is worth mentioning that the crystalline structures of the two C<sub>2</sub>N<sub>2</sub> materials are quite different from the above typical monolayer-structured C<sub>x</sub>N<sub>y</sub>, since there are two atomic layers in the unit cells of c-C<sub>2</sub>N<sub>2</sub> and h-C<sub>2</sub>N<sub>2</sub>. As shown in Fig. 15, both of them are constituted by two g-CN layers connected with C–C bonds, while the stacking modes of the layers are different. As a result, C atoms exhibit  $sp^3$  hybridization and N atoms are  $sp^2$  hybridized in both the c-C<sub>2</sub>N<sub>2</sub> and h-C<sub>2</sub>N<sub>2</sub> frameworks. According to the calculation results, c-C<sub>2</sub>N<sub>2</sub> and h-C<sub>2</sub>N<sub>2</sub> are wide-band semiconductors with the bandgaps of 4.43 and 3.70 eV, respectively.

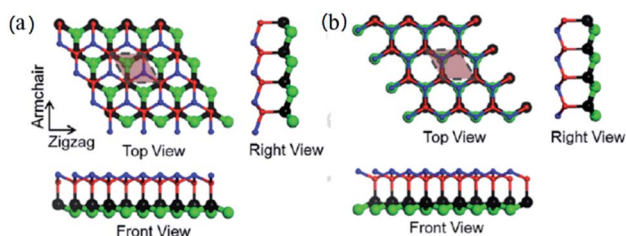


Fig. 15 Lattice structures of c-C<sub>2</sub>N<sub>2</sub> (a) and h-C<sub>2</sub>N<sub>2</sub> (b). Carbon atoms are colored with black in the bottom layer and red in the top layer. Nitrogen atoms are colored with green in the bottom layer and blue in the top layer. Reprinted with permission from ref. 14 copyright 2018 Elsevier B.V.

Meanwhile, good mechanical strength and high thermal conductivity of the two C<sub>x</sub>N<sub>y</sub> are also predicted. Unfortunately, the synthesis of the two structures has not been realized yet in the laboratory to provide experimental confirmation.

### 5.2 C<sub>2</sub>N<sub>3</sub>

Recently, Shi *et al.*<sup>73</sup> firstly studied the structural characteristics of C<sub>2</sub>N<sub>3</sub> and its structural stability and strain behavior by DFT calculations. The C<sub>2</sub>N<sub>3</sub> monolayer is a kind of carbon nitride with a C/N ratio of 2/3, which has the calculated lattice contents of  $a = 7.846$  Å and  $c = 6.549$  Å with a  $P6/mcm$  space group (Fig. 1). The bond lengths are 1.366 Å, 1.360 Å, and 1.340 Å for the N(1)–C(1), N(2)–C(1) and N(3)–C(1), respectively. The C<sub>2</sub>N<sub>3</sub> monolayer exhibits a typical p-type semiconductor behavior and good structural stability with Poisson's ratios of 0.39 and 0.27 in zigzag and armchair forms, respectively.

### 5.3 C<sub>5</sub>N

Wu *et al.*<sup>74</sup> used the *ab initio* evolutionary algorithm method to calculate four kinds of thermodynamically stable C<sub>5</sub>N phases ( $P62m$  (Fig. 1),  $R3m1$ ,  $R3m2$  and  $C2/m$ ). To explore the stability of the new phases, they carried out simulations under a high pressure of 100 GPa and the mechanical properties and evaluated the hardness of these phases. Moreover, the electronic properties, energy bandgap and band structure of the C<sub>5</sub>N were calculated.  $R3m1$ ,  $R3m2$  and  $C2/m$  phases are semiconducting with the bandgaps of 5, 5 and 2.15 eV, respectively, while  $P62m$  shows a metallic character.

### 5.4 C<sub>5</sub>N<sub>2</sub>

The C<sub>5</sub>N<sub>2</sub> monolayer has a similar porous crystalline structure to the C<sub>2</sub>N monolayer, except that the primitive cell of the C<sub>5</sub>N<sub>2</sub> is constituted by five fused benzene-like rings (three fused rings for C<sub>2</sub>N) bridged by pyrazine N (Fig. 16).<sup>75</sup> Accordingly, the primitive cell of C<sub>5</sub>N<sub>2</sub> contains 30 C atoms and 12 N atoms (CN stoichiometric ratio of 5 : 2) and the optimized lattice

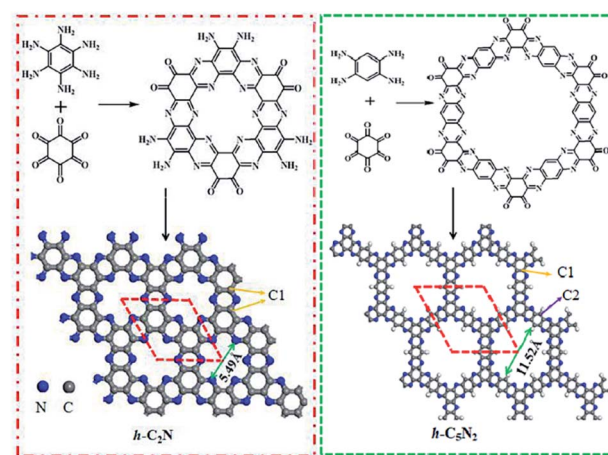


Fig. 16 Schematic representation of the synthesis of C<sub>2</sub>N and C<sub>5</sub>N<sub>2</sub> and graphic representation of a one-layer-conjugated skeleton. Reprinted with permission from ref. 75 copyright 2019 Elsevier B.V.

Table 1 Summary of the physicochemical properties, synthesis methods and potential applications of 2D  $C_xN_y$ <sup>a</sup>

$C_xN_y$	Bandgap/eV	Hole size/Å	Synthesis methods	Potential applications	Ref.
$g-C_3N_4$	2.70	6.8	Thermal reactions Solvothermal reactions Chemical vapor deposition Sol-gel synthesis Microwave heating	Water splitting CO <sub>2</sub> reduction Organic contaminant purification Fuel cells	15a and 78
$g-CN$	2.73	—	Solvothermal approach	Water splitting Hydrogen storage	41 and 72b 71
$C_2N$	1.96	8.3	Wet-chemical reaction Solid phase methods	Water splitting CO oxidation CO <sub>2</sub> RR NRR Gas adsorption/separation Fuel cells FET	19, 23, 38 and 39–41 16b, 34, 39 and 43 46 and 47 48 49 13a 9a
$C_3N$	2.67	Non-holey	Thermal reactions Hydrothermal method	Water splitting Fuel cells Gas adsorbent	57 and 58 59–61 62–66
$c-C_2N_2$	4.43	Non-holey	—	—	14
$h-C_2N_2$	3.70	Non-holey	—	—	—
$C_2N_3$	3.26	—	—	—	73
$C_5N$ (P62m)	0	Non-holey	—	—	74
$C_5N_2$	1.1	11.52	Reversible imine condensation reaction	Photocatalysis	76 and 77

<sup>a</sup> —: unknown.

parameter and the pore diameter are derived to be 16.59 Å and 11.52 Å, respectively, larger than those of  $C_2N$ .<sup>75</sup> Due to the nanoporosity of  $C_5N_2$ , it is also called holey  $C_5N_2$  ( $h-C_5N_2$ ). Theoretical calculations suggested that  $C_5N_2$  is also a semiconductor and that the bandgap of a  $C_5N_2$  monolayer is computed to be 1.10 eV, lower than that of a  $C_2N$  monolayer (1.72 eV).<sup>76</sup>

Very recently, the successful preparation of 2D multilayered  $C_5N_2$  was reported by Kim *et al.*<sup>77</sup> In their work, 1,2,4,5-benzenetetramine and hexaketocyclohexane were used as precursors. An efficient reversible imine condensation reaction was triggered by exposing the mixture under simulated sunlight irradiation for 3 h. Meanwhile, the electrical property measurement on the pellet of as-prepared 2D  $C_5N_2$  crystals showed that 2D  $C_5N_2$  crystals are semiconducting with a conductivity of  $2.22 \times 10^{-3} \text{ S m}^{-1}$ . Furthermore, the 2D  $C_5N_2$  film was observed to exhibit a rapid photo-response to white light irradiation, suggesting its potential in photocatalysis.

## 6. Summary and outlook

Over the last few years, 2D  $C_xN_y$  nanocrystals have attracted great interest arising from their graphene-like structure, open bandgap, large SSA, good chemical stability, and tunable surface chemistry, which enable plentiful applications in the areas of electronics, photocatalysis, electrocatalysis, energy storage devices, and gas adsorption/separation. In the 2D  $C_xN_y$  family,  $C_2N$ ,  $C_3N$  and  $C_5N_2$  have been successfully synthesized, while the other members including  $g-CN$ ,  $c-C_2N_2$ ,  $h-C_2N_2$  and  $C_5N$  are only theoretically predicted thus far. Among them,  $C_2N$  has been mostly studied because of its suitable bandgap and

unique nanoporous structure, which make it a potential photocatalyst, catalyst support for SACs and double-atom catalysts and membrane materials.<sup>79</sup> With the semiconducting electronic properties, face termination for electron localization, high SSA, 2D  $C_xN_y$  almost possess all the prerequisites as nonmetal heterogeneous catalysts. Additionally, the abundantly distributed Lewis basic functions and Brønsted basic functions originating from the electronegativity differences between N and C atoms in the  $C_xN_y$  framework can serve as catalytic sites for diverse reactions. In fact,  $g-C_3N_4$  has already been reported to be an excellent metal-free catalyst for organic reactions and cyclisation of functional nitriles.<sup>80</sup> Thereby, 2D  $C_xN_y$  materials are also promising metal-free heterogeneous catalysts and relevant studies deserve to be conducted in future. Hence, a vast amount of efforts has been devoted to the applications of  $C_2N$  in photocatalytic water splitting, multiple electrocatalytic reactions involving the ORR, HER, CO<sub>2</sub>RR, and NRR, as well as gas adsorption/separation. Compared to  $C_2N$ ,  $C_3N$  possesses a narrower bandgap but better electronic conductivity, which makes  $C_3N$  promising for not only photocatalysis and electrocatalysis but also battery electrodes. As for  $g-CN$ ,  $c-C_2N_2$ ,  $h-C_2N_2$ ,  $C_5N$  and  $C_5N_2$ , their possible applications are rather limited in the literature. A summary of the physicochemical properties, synthesis methods and potential applications of 2D  $C_xN_y$  is presented in Table 1. Albeit with the considerable progress on 2D CNs, there are still challenges that should be addressed in further work:

(i) The currently used precursors for  $C_xN_y$  synthesis are relatively expensive and some of the available synthetic strategies are complex and require strict experimental conditions,

which limit the large-scale production and practical applications. This is also the reason that a majority of the 2D  $C_xN_y$  compounds are theoretically investigated. Consequently, it is urgent to develop low-cost and easy-operation methods to fabricate 2D  $C_xN_y$  crystals.

(ii) Most of the obtained 2D  $C_xN_y$  crystals are in multilayered structure, while the layer number greatly affects the physico-chemical properties of  $C_xN_y$  and thus their applications. Hence, preparation of single-layered and few-layered  $C_xN_y$  is of importance.

(iii) Surface modifications like creating defects, functionalizing with oxygenated groups, doping with heteroatoms, etc. are believed to have a vital influence on the electronic and catalytic properties of  $C_xN_y$ , while relevant experimental and theoretical studies are very limited so far. Therefore, rational surface engineering of 2D  $C_xN_y$  should also be paid attention for promoting their practical applications.

(iv) In light of the good gas adsorption/separation efficiency of 2D  $C_xN_y$  for small molecular gases including  $H_2$ , He, CO, and  $CO_2$ , adsorption of VOC molecules is more important. Especially, the nanopores in  $C_2N$ , g-CN and  $C_5N_2$  may be efficient for VOC separation. Doping  $C_xN_y$  with specific elements or building a composite material can enhance their selective adsorption towards gas molecules. Therefore, further attempts on the potential applications of 2D  $C_xN_y$  in adsorption are very promising.

(v) Since the good performance of  $C_2N$ - and  $C_3N$ -based photocatalysts for water splitting and the wide bandgap of g-CN, c- $C_2N_2$ , h- $C_2N_2$ ,  $C_5N$  and  $C_5N_2$  have been theoretically illustrated, 2D  $C_xN_y$  materials are also expected to hold potential in photocatalytic degradation of both aqueous organic pollutants and VOCs for environmental remediation. Moreover, large SSA and planar structures of 2D  $C_xN_y$  can possibly facilitate more exposure of active sites and adsorptive photocatalysis, beneficial to the photocatalytic degradation processes.

In summary, research on various 2D  $C_xN_y$  structures and their potential applications in different fields is still in its infancy. The challenges and various opportunities are huge for the scientific community to explore. We wish that the information provided in this review can attract increasing interest in the area of 2D  $C_xN_y$ .

## Conflicts of interest

There are no conflicts to declare.

## Acknowledgements

Li Tan and Chunyang Nie contributed equally to this work. This work was supported by the National Natural Science Foundation of China (No. 21777033 and 21806024), China Postdoctoral Science Foundation (No. 2017M622637), Science and Technology Planning Project of Guangdong Province (No. 2017B020216003), Innovation Team Project of Guangdong Provincial Department of Education (No. 2017KCXTD012), and Australian Research Council (DP170104264).

## References

- 1 K. S. Novoselov, A. K. Geim, S. V. Morozov, D. Jiang, Y. Zhang, S. V. Dubonos, I. V. Grigorieva and A. A. Firsov, *Science*, 2004, **306**, 666.
- 2 X. Du, I. Skachko, A. Barker and E. Y. Andrei, *Nat. Nanotechnol.*, 2008, **3**, 491.
- 3 (a) D. Sun, D. Ye, P. Liu, Y. Tang, J. Guo, L. Wang and H. Wang, *Adv. Energy Mater.*, 2018, **8**, 1702383; (b) J. Mao, J. Iocozzia, J. Huang, K. Meng, Y. Lai and Z. Lin, *Energy Environ. Sci.*, 2018, **11**, 772; (c) K.-Q. Lu, X. Xin, N. Zhang, Z.-R. Tang and Y.-J. Xu, *J. Mater. Chem. A*, 2018, **6**, 4590.
- 4 K. C. Kemp, H. Seema, M. Saleh, N. H. Le, K. Mahesh, V. Chandra and K. S. Kim, *Nanoscale*, 2013, **5**, 3149.
- 5 J. B. Wu, M. L. Lin, X. Cong, H. N. Liu and P. H. Tan, *Chem. Soc. Rev.*, 2018, **47**, 1822.
- 6 (a) M. Terrones, A. R. Botello-Méndez, J. Campos-Delgado, F. López-Urías, Y. I. Vega-Cantú, F. J. Rodríguez-Macías, A. L. Elías, E. Muñoz-Sandoval, A. G. Cano-Márquez and J.-C. Charlier, *Nano Today*, 2010, **5**, 351; (b) A. Chuvilin, E. Bichoutskaia, M. C. Gimenez-Lopez, T. W. Chamberlain, G. A. Rance, N. Kuganathan, J. Biskupek, U. Kaiser and A. N. Khlobystov, *Nat. Mater.*, 2011, **10**, 687; (c) L. Jia, D.-H. Wang, Y. X. Huang, A. W. Xu and H. Q. Yu, *J. Phys. Chem. C*, 2011, **115**, 11466.
- 7 (a) W. Dacheng, L. Yunqi, W. Yu, Z. Hongliang, H. Liping and Y. Gui, *Nano Lett.*, 2009, **9**, 1752; (b) Z. M. Ao and F. M. Peeters, *J. Phys. Chem. C*, 2010, **114**, 14503.
- 8 H. Wang, T. Maiyalagan and X. Wang, *ACS Catal.*, 2012, **2**, 781.
- 9 (a) J. Mahmood, E. K. Lee, M. Jung, D. Shin, I. Y. Jeon, S. M. Jung, H. J. Choi, J. M. Seo, S. Y. Bae, S. D. Sohn, N. Park, J. H. Oh, H. J. Shin and J. B. Baek, *Nat. Commun.*, 2015, **6**, 6486; (b) R. Walczak, B. Kurpil, A. Savateev, T. Heil, J. Schmidt, Q. Qin, M. Antonietti and M. Oschatz, *Angew. Chem., Int. Ed.*, 2018, **57**, 10765; (c) J. Li, Y. Li, Z. Xiong, G. Yao and B. Lai, *Chin. Chem. Lett.*, 2019, **30**, 2139.
- 10 A. Y. Liu and M. L. Cohen, *Science*, 1989, **245**, 841.
- 11 X. Wang, K. Maeda, X. Chen, K. Takane, K. Domen, Y. Hou, X. Fu and M. Antonietti, *J. Am. Chem. Soc.*, 2009, **131**, 1680.
- 12 (a) M. Z. Rahman, K. Davey and C. B. Mullins, *Adv. Sci.*, 2018, **5**, 1800820; (b) F. Yu, L. Wang, Q. Xing, D. Wang, X. Jiang, G. Li, A. Zheng, F. Ai and J. P. Zou, *Chin. Chem. Lett.*, 2020, **31**, 1648; (c) M. Wu, H. Lv, T. Wang, Z. Ao, H. Sun, C. Wang, T. An and S. Wang, *Catal. Today*, 2018, **315**, 205.
- 13 (a) J. Xu, J. Mahmood, Y. Dou, S. Dou, F. Li, L. Dai and J. B. Baek, *Adv. Mater.*, 2017, **29**, 1702007; (b) S. Yang, W. Li, C. Ye, G. Wang, H. Tian, C. Zhu, P. He, G. Ding, X. Xie, Y. Liu, Y. Lifshitz, S. T. Lee, Z. Kang and M. Jiang, *Adv. Mater.*, 2017, **29**, 1605625.
- 14 Y. Dong, C. Zhang, M. Meng, M. M. Groves and J. Lin, *Carbon*, 2018, **138**, 319.
- 15 (a) S. Ye, R. Wang, M.-Z. Wu and Y.-P. Yuan, *Appl. Surf. Sci.*, 2015, **358**, 15; (b) M. Wu, X. He, B. Jing, T. Wang, C. Wang,

- Y. Qin, Z. Ao, S. Wang and T. An, *J. Hazard. Mater.*, 2020, **384**, 121323.
- 16 (a) X. Li, L. Zhu, Q. Xue, X. Chang, C. Ling and W. Xing, *ACS Appl. Mater. Interfaces*, 2017, **9**, 31161; (b) F. Li and Z. Chen, *Nanoscale*, 2018, **10**, 15696.
- 17 (a) O. Y. Podyacheva, D. A. Bulushev, A. N. Suboch, D. A. Svintsitskiy, A. S. Lisitsyn, E. Modin, A. Chuvilin, E. Y. Gerasimov, V. I. Sobolev and V. N. Parmon, *ChemSusChem*, 2018, **11**, 3724; (b) Y. Chen, S. Ji, Y. Wang, J. Dong, W. Chen, Z. Li, R. Shen, L. Zheng, Z. Zhuang, D. Wang and Y. Li, *Angew. Chem., Int. Ed.*, 2017, **56**, 6937; (c) G. Liu, J. Zhou, W. Zhao, Z. Ao and T. An, *Chin. Chem. Lett.*, 2020, **31**, 1966.
- 18 T. Komatsu and M. Samejima, *J. Mater. Chem.*, 1998, **8**, 193.
- 19 S. S. Shinde, C. H. Lee, J. Y. Yu, D. H. Kim, S. U. Lee and J. H. Lee, *ACS Nano*, 2018, **12**, 596.
- 20 S. Gong, W. Wan, S. Guan, B. Tai, C. Liu, B. Fu, S. A. Yang and Y. Yao, *J. Mater. Chem. C*, 2017, **5**, 8424.
- 21 J. Du, C. Xia, W. Xiong, X. Zhao, T. Wang and Y. Jia, *Phys. Chem. Chem. Phys.*, 2016, **18**, 22678.
- 22 X. Xie, Z. Ao, D. Su, J. Zhang and G. Wang, *Adv. Funct. Mater.*, 2015, **25**, 1393.
- 23 J. Mahmood, S.-M. Jung, S. J. Kim, J. Park, J.-W. Yoo and J.-B. Baek, *Chem. Mater.*, 2015, **27**, 4860.
- 24 N. Fechner, N. P. Zussblatt, R. Rothe, R. Schlogl, M. G. Willinger, B. F. Chmelka and M. Antonietti, *Adv. Mater.*, 2016, **28**, 1287.
- 25 T. Jordan, M. Shalom, M. Antonietti and N. Fechner, *Asia-Pac. J. Chem. Eng.*, 2016, **11**, 866.
- 26 D. Li, X.-a. Ning, Y. Huang and S. Li, *Electrochim. Acta*, 2019, **312**, 251.
- 27 X. Cui, W. An, X. Liu, H. Wang, Y. Men and J. Wang, *Nanoscale*, 2018, **10**, 15262.
- 28 Y. Liu, Z. Meng, X. Guo, G. Xu, D. Rao, Y. Wang, K. Deng and R. Lu, *Phys. Chem. Chem. Phys.*, 2017, **19**, 28323.
- 29 J. Zhu, M. Zulfiqar, S. Zeng, Y. Zhao and J. Ni, *AIP Adv.*, 2018, **8**, 055333.
- 30 J. Du, C. Xia, T. Wang, W. Xiong and J. Li, *J. Mater. Chem. C*, 2016, **4**, 9294.
- 31 Y. Bai, Q. Zhang, N. Xu, K. Deng and E. Kan, *J. Phys. Chem. C*, 2018, **122**, 15892.
- 32 C. Zhang, Y. Jiao, T. He, S. Bottle, T. Frauenheim and A. Du, *J. Phys. Chem. Lett.*, 2018, **9**, 858.
- 33 H. Wang, X. Li and J. Yang, *Chemphyschem*, 2016, **17**, 2100.
- 34 D. W. Ma, Q. Wang, X. Yan, X. Zhang, C. He, D. Zhou, Y. Tang, Z. Lu and Z. Yang, *Carbon*, 2016, **105**, 463.
- 35 R. Zhang, B. Li and J. Yang, *Nanoscale*, 2015, **7**, 14062.
- 36 R. Longuinhas and J. Ribeiro-Soares, *Phys. Rev. B*, 2018, **97**, 195119.
- 37 R. Zhang and J. Yang, 2015, arXiv:1505.02768.
- 38 R. Zhang, L. Zhang, Q. Zheng, P. Gao, J. Zhao and J. Yang, *J. Phys. Chem. Lett.*, 2018, **9**, 5419.
- 39 M. Makaremi, S. Grixti, K. T. Butler, G. A. Ozin and C. V. Singh, *ACS Appl. Mater. Interfaces*, 2018, **10**, 11143.
- 40 J. Mahmood, F. Li, S. M. Jung, M. S. Okyay, I. Ahmad, S. J. Kim, N. Park, H. Y. Jeong and J. B. Baek, *Nat. Nanotechnol.*, 2017, **12**, 441.
- 41 X. Li, P. Cui, W. Zhong, J. Li, X. Wang, Z. Wang and J. Jiang, *Chem. Commun.*, 2016, **52**, 13233.
- 42 X. Zhang, A. Chen, Z. Zhang, M. Jiao and Z. Zhou, *J. Mater. Chem. A*, 2018, **6**, 11446.
- 43 (a) B. L. He, J. S. Shen and Z. X. Tian, *Phys. Chem. Chem. Phys.*, 2016, **18**, 24261; (b) S. Chakrabarty, T. Das, P. Banerjee, R. Thapa and G. P. Das, *Appl. Surf. Sci.*, 2017, **418**, 92.
- 44 (a) Q. Jiang, J. Zhang, Z. Ao, H. Huang, H. He and Y. Wu, *Front. Chem.*, 2018, **6**, 187; (b) C. Li, Y. Xu, W. Sheng, W. J. Yin, G. Z. Nie and Z. Ao, *Phys. Chem. Chem. Phys.*, 2020, **22**, 615.
- 45 Q. Jiang, J. Zhang, H. Huang, Y. Wu and Z. Ao, *J. Mater. Chem. A*, 2020, **8**, 287.
- 46 J. Zhao, J. Zhao, F. Li and Z. Chen, *J. Phys. Chem. C*, 2018, **122**, 19712.
- 47 Z. Wang, Z. Yu and J. Zhao, *Phys. Chem. Chem. Phys.*, 2018, **20**, 12835.
- 48 X. Zhang, A. Chen, Z. Zhang and Z. Zhou, *J. Mater. Chem. A*, 2018, **6**, 18599.
- 49 (a) B. Xu, H. Xiang, Q. Wei, J. Q. Liu, Y. D. Xia, J. Yin and Z. G. Liu, *Phys. Chem. Chem. Phys.*, 2015, **17**, 15115; (b) A. Hashmi, M. U. Farooq, I. Khan, J. Son and J. Hong, *J. Mater. Chem. A*, 2017, **5**, 2821; (c) Z. Hu, B. Liu, M. Dahanayaka, A. W. Law, J. Wei and K. Zhou, *Phys. Chem. Chem. Phys.*, 2017, **19**, 15973; (d) W. Ralf, K. Bogdan, S. Aleksandr, H. Tobias, S. Johannes, Q. Qing, A. Markus and O. M. J. A. Chemie, *Angew. Chem., Int. Ed.*, 2018, **57**, 10765; (e) Y. Su, Z. Ao, Y. Ji, G. Li and T. An, *Appl. Surf. Sci.*, 2018, **450**, 484; (f) L. Zhu, Q. Xue, X. Li, T. Wu, Y. Jin and W. Xing, *J. Mater. Chem. A*, 2015, **3**, 21351.
- 50 Y. Su, W. Li, G. Li, Z. Ao and T. An, *Chin. J. Catal.*, 2019, **40**, 664.
- 51 (a) É. Sandré, C. J. Pickard and C. Colliex, *Chem. Phys. Lett.*, 2000, **325**, 53; (b) Q. Hu, Q. Wu, H. Wang, J. He and G. Zhang, *Phys. Status Solidi B*, 2012, **249**, 784.
- 52 (a) G. Sun, Z. Y. Liu and J. L. He, *Chin. Phys. Lett.*, 2007, **24**, 1092; (b) L. L. Pang, J. Q. Bi, Y. J. Bai, Y. X. Qi, H. L. Zhu, C. G. Wang, J. W. Wu and C. W. Lu, *Mater. Chem. Phys.*, 2008, **112**, 1124.
- 53 J. Mahmood, E. K. Lee, M. Jung, D. Shin, H. J. Choi, J. M. Seo, S. M. Jung, D. Kim, F. Li, M. S. Lah, N. Park, H. J. Shin, J. H. Oh and J. B. Baek, *Proc. Natl. Acad. Sci. U. S. A.*, 2016, **113**, 7414.
- 54 S. Kumar, S. Sharma, V. Babar and U. Schwingenschlögl, *J. Mater. Chem. A*, 2017, **5**, 20407.
- 55 T. C. King, P. D. Matthews, J. P. Holgado, D. A. Jefferson, R. M. Lambert, A. Alavi and D. S. Wright, *Carbon*, 2013, **64**, 6.
- 56 (a) X. Zhou, W. Feng, S. Guan, B. Fu, W. Su and Y. Yao, *J. Mater. Res.*, 2017, **32**, 2993; (b) X. Wang, Q. Li, H. Wang, Y. Gao, J. Hou and J. Shao, *Phys. B*, 2018, **537**, 314.
- 57 J. Wang, X. Li, Y. You, X. Yang, Y. Wang and Q. Li, *Nanotechnology*, 2018, **29**, 365401.
- 58 X. Niu, X. Bai, Z. Zhou and J. Wang, *ACS Catal.*, 2020, **10**, 1976.
- 59 (a) W. Xu, C. Chen, C. Tang, Y. Li and L. Xu, *Sci. Rep.*, 2018, **8**, 5661; (b) H. Bingling, S. Jiansheng, M. Dongwei,

- L. Zhansheng and Y. Zongxian, *J. Phys. Chem. C*, 2018, **122**, 20312; (c) Y. Zhou, G. Gao, J. Kang, W. Chu and L. W. Wang, *J. Mater. Chem. A*, 2019, **7**, 12050.
- 60 Q. Liu, B. Xiao, J. B. Cheng, Y. C. Li, Q. Z. Li, W. Z. Li, X. F. Xu and X. F. Yu, *ACS Appl. Mater. Interfaces*, 2018, **10**, 37135.
- 61 P. Bhauriyal, A. Mahata and B. Pathak, *J. Phys. Chem. C*, 2018, **122**, 2481.
- 62 C. H. Yu, C. H. Huang and C. S. Tan, *Aerosol Air Qual. Res.*, 2012, **12**, 745.
- 63 D. Ma, J. Zhang, X. Li, C. He, Z. Lu, Z. Lu, Z. Yang and Y. Wang, *Sens. Actuators, B*, 2018, **266**, 664.
- 64 I. Choudhuri, N. Patra, A. Mahata, R. Ahuja and B. Pathak, *J. Phys. Chem. C*, 2015, **119**, 24827.
- 65 M. Pashangpour and A. A. Peyghan, *J. Mol. Model.*, 2015, **21**, 116.
- 66 (a) G. Qin, Q. Cui, W. Wang, P. Li, A. Du and Q. Sun, *Chemphyschem*, 2018, **19**, 2788; (b) X. Li, T. Guo, L. Zhu, C. Ling, Q. Xue and W. Xing, *Chem. Eng. J.*, 2018, **338**, 92.
- 67 L. B. Shi, Y. Y. Zhang, X. M. Xiu and H. K. Dong, *Carbon*, 2018, **134**, 103.
- 68 H. W. Kim, H. W. Yoon, S. M. Yoon, B. M. Yoo, B. K. Ahn, Y. H. Cho, H. J. Shin, H. Yang, U. Paik and S. J. S. Kwon, *Science*, 2013, **342**, 91.
- 69 X. Ma, L. Li, Z. Zeng, R. Chen, C. Wang, K. Zhou, C. Su and H. Li, *Chem. Eng. J.*, 2019, **363**, 49.
- 70 J. Li, C. Cao, J. Hao, H. Qiu, Y. Xu and H. Zhu, *Diamond Relat. Mater.*, 2006, **15**, 1593.
- 71 Y. D. Chen, S. Yu, W. H. Zhao, S. F. Li and X. M. Duan, *Phys. Chem. Chem. Phys.*, 2018, **20**, 13473.
- 72 (a) K. Srinivasu and S. K. Ghosh, *J. Mater. Chem. A*, 2015, **3**, 23011; (b) K. Srinivasu, B. Modak and S. K. Ghosh, *J. Phys. Chem. C*, 2014, **118**, 26479.
- 73 L. B. Shi, S. Cao, J. Zhang, X. M. Xiu and H.-K. Dong, *Phys. E*, 2018, **103**, 252.
- 74 Q. Wu, Q. Hu, Y. Hou, H. Wang, A. Zhou and L. Wang, *J. Phys.: Condens. Matter*, 2018, **30**, 385402.
- 75 C. Yang, Z.-D. Yang, R. Zhang and G. Zhang, *Chem. Phys.*, 2019, **517**, 104.
- 76 Z. D. Yang, W. Wu and X. C. Zeng, *J. Mater. Chem. C*, 2014, **2**, 2902.
- 77 S. Kim and H. C. Choi, *Commun. Chem.*, 2019, **2**, 60.
- 78 W. K. Darkwah and Y. Ao, *Nanoscale Res. Lett.*, 2018, **13**, 388.
- 79 W. Yao, Y. Zhang, H. Zhu, C. Ge and D. Wang, *Chin. Chem. Lett.*, 2020, **31**, 701.
- 80 T. Wang, C. Nie, Z. Ao, S. Wang and T. An, *J. Mater. Chem. A*, 2020, **8**, 485.